1

Basic Fundamentals of Digital Holography

The idea of digitally reconstructing the optical wavefront first appeared in the 1960s. The oldest study on the subject dates back to 1967 with the article published by Goodman in *Applied Physics Letters* [GOO 67]. The aim was to replace the "analog" recording/decoding of the object by a "digital" recording/decoding simulating diffraction from a digital grating consisting of the recorded image. Thus, holography became "digital", replacing the silvered support with a matrix of the discrete values of the hologram. Then, in 1971, Huang discussed the computer analysis of optical wavefronts and introduced for the first time the concept of "digital holography" [HUA 71]. The works presented in 1972 by Kronrod [KRO 72] historically constituted the first attempts at reconstruction by the calculation of an object coded in a hologram. At that time, 6 h of calculation was required for the reconstruction of a field of 512×512 pixels with the Minsk-22 computer, the discrete values being obtained from a holographic plate by 64-bit digitization with a scanner. However, it took until the 1990s for array detector-based digital holography to materialize [SCH 94]. In effect, there have been important developments in two sectors of technology: since this period, microtechnological processes have resulted in charge coupled device (CCD) arrays with sufficiently small pixels to fulfill the Shannon condition for the spatial sampling of a hologram; the

Chapter written by Pascal PICART, Michel GROSS and Pierre MARQUET.

computational treatment of images has become accessible largely due to the significant improvement in microprocessor performance, in particular their processing units as well as storage capacities.

The physical principle of digital holography is similar to that of traditional holography. However, the size of the pixels in an image detector (CCD or complementary metal oxyde semiconductor (CMOS)) is clearly greater than that of the grains of a traditional photographic plate (typically 2–3 μm, compared with some 25 nm). These constraints impose to take into account certain parameters (pixel area, number of pixels and pixel pitch) which were more or less clear in an analog holography.

This chapter, as an introduction to advanced methods detailed in other chapters, aims at describing the different aspects related to digital holography: the principle of light diffraction, how to record a digital hologram and color holograms, algorithms to reconstruct digital holograms, an insight into the different holographic configurations, special techniques to demodulate the hologram, the basic principle of digital holographic interferometry and a brief discussion on tomographic phase imaging.

1.1. Digital holograms

A digital hologram is an interferometric mixing between a reference wave and a wave from the object of interest. This section presents the basic properties related to a digital hologram.

1.1.1. *Interferences between the object and reference waves*

Figure 1.1 illustrates the basic geometry for recording a digital hologram. An object wave is coherently mixed with a reference wave, and their interferences are recorded in the recording plane H. In digital holography, the recording is performed by using a pixel matrix sensor.

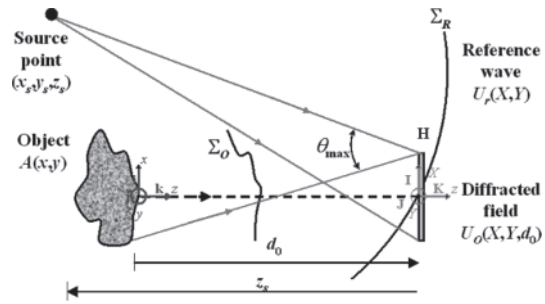

Figure 1.1. *Free space diffraction, interferences and notations. For a color version of this figure, see www.iste.co.uk/picart/digiholography.zip*

Consider an extended object illuminated with a monochromatic wave. This object diffracts a wave to the observation plane localized at a distance $d_0 = |z_0|$. The surface of the object generates a wavefront which will be denoted as A ($i = \sqrt{-1}$):

$$A(x,y) = A_0(x,y)\exp\left(i\psi_0(x,y)\right). \qquad [1.1]$$

The amplitude A_0 describes the reflectivity/transmission of the object and phase ψ_0 is related to its surface and shape or thickness and refractive index. Because of the natural roughness of the object, ψ_0 is a random variable, uniformly distributed over $[-\pi,+\pi]$. The diffracted field U_O at distance d_0, and at spatial coordinates (X,Y) of the observation plane, is given by the propagation of the object wave to the recording plane. In the observation plane, this wave can be simply written as:

$$U_O(X,Y,d_0) = a_O(X,Y)\exp\left(i\phi_O(X,Y)\right), \qquad [1.2]$$

here a_O is the modulus of the complex amplitude and φ_O is its optical phase. Since the object is naturally rough, the diffracted field at distance d_0 is a speckle pattern [DAI 84, GOO 07].

Let us consider U_r, the complex amplitude of the reference wavefront, at the recording plane. We have:

$$U_r(X,Y) = a_r(X,Y)\exp\left(i\phi_r(X,Y)\right), \qquad [1.3]$$

where a_r is the modulus and φ_r is the optical phase. The reference wavefront usually comes from a small pinhole: thus, it is a spherical divergent wave, impacting the plane with a non-zero incident angle. Considering (x_s, y_s, z_s) the coordinates of the source point in the hologram reference frame ($z_s<0$), the optical phase of the reference wave can be written in the paraxial approximations by [GOO 72, GOO 05]:

$$\phi_r(X,Y) \cong \frac{\pi}{\lambda z_s}\left((X-x_s)^2+(Y-y_s)^2\right). \quad [1.4]$$

This optical phase can also be written as:

$$\phi_r(X,Y) = 2\pi(u_0 X + v_0 Y) + \frac{\pi}{\lambda z_s}\left(X^2+Y^2\right)+\phi_s, \quad [1.5]$$

where (u_0,v_0) are the carrier spatial frequencies of the hologram, and φ_s is a constant term that can be omitted. When $(u_0,v_0) = (0,0)$, i.e. reference point source localized on the z-axis, holography is said to be "in-line" (no tilt between the two waves), whereas when $(u_0,v_0) \neq (0,0)$, holography is said to be "off-axis" (slight tilt between the two waves). As a general rule, we are interested in adjusting the reference wave so that it has uniform amplitude, i.e. $a_r(X,Y) = C^{te}$. The total illumination, denoted H, is then written as [KRE 96, HAR 02, KRE 04]:

$$H = |U_r + U_O|^2 = |U_r|^2 + |U_O|^2 + U_r^* U_O + U_r U_O^*. \quad [1.6]$$

This equation can also be written as:

$$H = a_r^2 + a_O^2 + 2a_r a_O \cos(\phi_r - \phi_O). \quad [1.7]$$

Equations [1.6] and [1.7] constitute what is classically called the *digital hologram*. It includes *three orders*: the 0-order is composed of terms $|U_r|^2+|U_O|^2$, the +1 order is the term $U_r^* U_O$ and the −1 order is the term $U_r U^*_O$, also called the twin image. Generally, the +1 order is of interest because it is related to the initial object, whereas the −1 order exhibits some symmetry that is due to the hermitic property of the Fourier operator. Figure 1.2 shows a digital hologram and a zoom on one of its part.

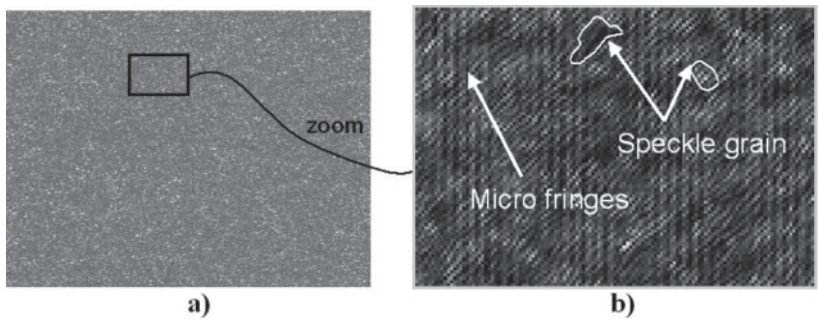

Figure 1.2. *Fine structure of a digital hologram: a) digitally recorded hologram and b) zoom showing micro fringes and speckle grains*

As can be seen, the microstructure of a digital hologram is composed of micro fringes, on the one hand, and light grains, on the other hand. These light grains are *speckles* that are due to the random nature of the light reflected from the object [GOO 85, DAI 84]. Note that in the case where the object is transparent and non-diffusing, the speckle nature of the hologram may disappear.

1.1.2. *Role of the image sensor*

1.1.2.1. *Spatial sampling and Shannon conditions*

In digital holography, the hologram is recorded with $N \times M$ pixels having pitches p_x and p_y and active surfaces Δ_x and Δ_y, respectively, for the x- and y-directions. Thus, the space coordinates in the recording plane are sampled; this means that we have $(X, Y) = (np_x, mp_y)$ with $(m; n) \in (-M/2,+M/2-1;-N/2,+N/2-1)$. In addition, the sampling of the hologram leads to Shannon conditions. Considering the maximum angle $\theta_{\max}$ (see Figure 1.1) between the two waves, the micro fringes locally produced by the two tilted wavefronts must be sampled so that the sampling pitch is at least equal to two times the fringe period. Thus, this leads to the maximum acceptable angle for the setup, according to the following equation [SCH 94]:

$$\theta_{\max} < 2\sin^{-1}\left(\frac{\lambda}{4\max\left(p_x, p_y\right)}\right). \qquad [1.8]$$

For example, with λ = 632.8 nm and $p_x = p_y$ = 4.65 μm, the maximum acceptable angle is smaller than 4°. This means that the setup must be precisely adjusted so as to fulfill the Shannon conditions.

1.1.2.2. *Low-pass filtering*

The digital hologram effectively recorded by the sensor is not simply described by equation [1.6]. Indeed, we must take into account the active surface of pixels, which induces a local spatial integration. So, the recorded hologram at point (np_x, mp_y) was given to be written as [PIC 08]:

$$H_{PIX}\left(np_x, mp_y\right) = \left[H\left(X,Y\right) * \Pi_{\Delta_x,\Delta_y}\left(X,Y\right)\right]\left(np_x, mp_y\right). \quad [1.9]$$

with the even pixel function:

$$\Pi_{\Delta_x,\Delta_y}\left(x,y\right) = \begin{cases} 1/\Delta_x \times 1/\Delta_y & \text{if} \quad |x| \le \Delta_x/2 \quad \text{and} \quad |y| \le \Delta_y/2 \\ 0 \quad \text{if not} \end{cases}. \quad [1.10]$$

From equation [1.9], the basic effect can be understood: since the pixel provides local integration of the micro fringes, the consequence is a blurring of these fringes. Qualitatively, this means that the spatial resolution will deteriorate and that the pixel induces a low-pass filtering to the digital hologram.

1.1.2.3. *Effect of the exposure time*

During the recording of the hologram, the pixel receives light for a certain duration, called the exposure time T. The total energy received by the sensor is such that [KRE 96]:

$$W = \int_{t_1}^{t_1+T} H\left(t\right) dt\,. \quad [1.11]$$

When the hologram has no temporal dependence, the time integration can be omitted. However, in the case where the object exhibits time dependence, i.e. sinusoidal oscillation, the exposure time

influences significantly the recorded hologram. The characteristic parameter of the recording is the cyclic ratio defined by $\alpha = T/T_0$, which is the ratio between the exposure time T and the oscillation period T_0. Typically, if $\alpha << 1$, the recording regime uses light pulses and is equivalent to a freezing of the object at the instant at which the recording is performed ("impulse regime") [LEC 13]. When, on the contrary, we have $\alpha >> 1$, the regime is said to be "time-averaging". The object reconstructed from the digital hologram is then amplitude-modulated by a Bessel function [PIC 03, PIC 05]. In experiments for which $0 << \alpha < 1$, the cyclic ratio is too high to be classified as "impulse" and too low to be considered as "time-averaging". This intermediary regime is called "quasi-time-averaging" and is completely described in [LEC 13]. The object amplitude also exhibits a modulation that is more complex than that of the pure time-averaging regime.

1.1.2.4. *Recording digital color holograms*

The first digital color holograms appeared in the 2000s with the advent of color detectors. Yamaguchi showed the applicability of digital color holography to the color reconstruction of objects [YAM 02]. Since then, numerous applications have been developed, particularly in the domain of contactless metrology: flow analysis in fluid mechanics [DEM 03, DES 08, DES 12], surface profilometry by two-color microscopy [KUM 09, KUH 07, MAN 08], three-color digital holographic microscopy (DHM) even with low coherence [DUB 12] and multidimensional metrology of deformed objects [KHM 08, TAN 10a, TAN 10b, TAN 11]. There are different approaches for recording digital color holograms, in particular for *simultaneously* recording the three colors. The simplest method consists of using a monochromatic detector and recording the colors *sequentially*. This method was proposed by Demoli in 2003 [DEM 03] and is only adapted to the case of objects which vary slowing in time. Figure 1.3 illustrates the different recording strategies. The first possibility consists of using a chromatic filter organized in a Bayer mosaic (Figure 1.3(a)). However, in such a detector, half of the pixels detect green, and only a quarter detect red or blue [YAM 02, DES 11].

The spatial color filter creates holes in the mesh, and therefore a loss of information, which translates into a loss of resolution. For example, Yamaguchi used a detector with 1,636 × 1,238 pixels of size 3.9 × 3.9 μm^2 [YAM 02], and his results had a relatively low spatial resolution. The number of pixels for each color was 818 × 619, and the pixel pitch was 7.8 μm. The second possibility consists of using three detectors organized as a "tri-CCD", the spectral selection being carried out by a prism with dichroic layers (Figure 1.3(b)). Such a detector guarantees a high spatial resolution and a spectral selectivity compatible with the constraints of digital color holography. Of course, the relative adjustment of the three sensors must be realized with high precision. For example, Desse developed a type of holographic color interferometry for use in fluid mechanics, with three detectors of 1,344 × 1,024 pixels of size 6.45 μm × 6.45 μm [DES 11]. The third possibility consists of using a color detector based on a stack of photodiodes [TAN 10a, TAN 10b, DES 08, DES 11] (http://www.foveon.com, Figure 1.3(c)). The spectral selectivity is relative to the mean penetration depth of the photons in the silicon: blue photons at 425 nm penetrate to around 0.2 μm, green photons at 532 nm to around 2 μm and red photons at 630 nm to around 3 μm. Thus, the construction of junctions at depths at around 0.2, 0.8 and 3.0 μm gives the correct spectral selectivity for color imaging. However, the spectral selectivity is not perfect, as green photons may be detected in the blue and red bands, but the architecture guarantees a maximum spectral resolution since the number of effective pixels for each wavelength is that of the entire matrix. For example, [TAN 10b] uses a stack of photodiodes with 1,060 × 1,414 pixels of size 5 × 5 μm^2. One last possibility consists of using a monochromatic detector combined with spatial chromatic multiplexing (Figure 1.3(d)). Each reference wave must have different separately adjusted spatial frequencies according to their wavelengths. The complexity of the experimental apparatus increases with the number of colors. For two-color digital holography, it is acceptable; for three colors, it becomes prohibitive. A demonstration of this approach is given in [PIC 09, MAN 08, KUH 07] and [TAN 11].

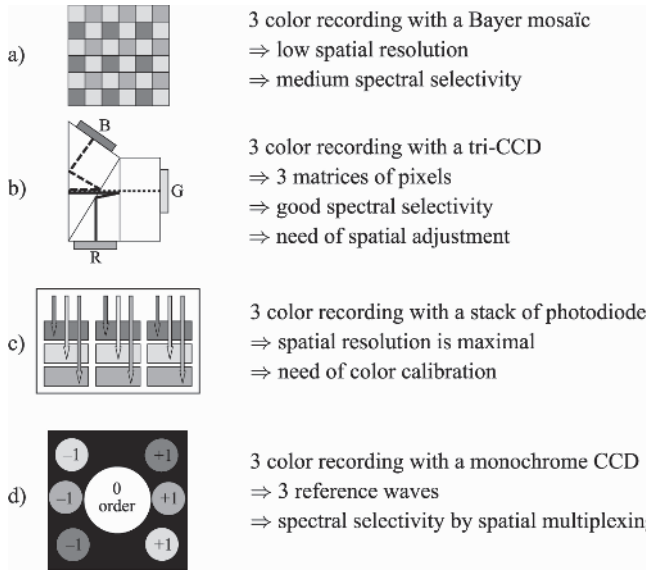

Figure 1.3. *Recording digital color holograms. For a color version of this figure, see www.iste.co.uk/picart/digiholography.zip*

1.1.3. *Demodulation of digital holograms*

Equations [1.6] and [1.7] describe the digital hologram. The +1 order is of interest because it includes the object wave through term $U_r^* U_O$. Note that the −1, $U_r U^*_O$, is the complex conjugate of $U_r^* U_O$ and that it includes also the full information on the object wave. The demodulation of the digital hologram consists of retrieving the +1 order from the recording of H. There are mainly two ways to perform demodulation: using slightly off-axis geometry at the recording, or using phase-shifting [CUC 99b]. These approaches are detailed in the next sections.

1.1.3.1. *Off-axis holograms*

Off-axis geometry introduces a spatial carrier frequency and demodulation restores the full spatial frequency content of the wavefront, i.e. $U_r^* U_O$. In equation [1.5], the phase of the reference wave includes the carrier spatial frequencies of the hologram (u_0,v_0). When $(u_0,v_0) \neq (0,0)$, there is a slight tilt between the two waves and

holography is off-axis. Practically, the different diffraction terms encoded in the hologram (zero-order wave, real image and virtual image) are propagating in different directions, enabling their separation for reconstruction. This configuration was the one employed for the first demonstration of a fully numerical recording and reconstruction holography [SCH 94, COQ 95]. In practice, reconstruction methods based on off-axis configuration usually rely on Fourier methods to filter one of the diffraction terms contained in the hologram ($U_r^* U_O$ or $U_r U^*_O$) [CUC 00]. This concept was first proposed by Takeda *et al.* [TAK 82] in the context of interferometric topography. The method was later extended for smooth topographic measurements for phase recovery [KRE 86] and generalized for the use in DHM with amplitude and phase recovery [CUC 99a].

According to equations [1.3]–[1.6], in the spatial frequency spectrum, a three-modal distribution is related to the three diffraction orders of the hologram (*FT* and FT^{-1} means, respectively, Fourier transform and inverse Fourier transform):

$$FT[H](u,v) = C_0(u,v) + C_1(u-u_0, v-v_0) + C_1^*(-u-u_0, -v-v_0), \qquad [1.12]$$

where C_0 is the Fourier transform of the zero-order and C_1 is the Fourier transform of the +1 order. If the three orders are well separated in the Fourier plane, the +1 order can be extracted from the Fourier spectrum. Figure 1.4 illustrates the spectral distribution in the Fourier domain of the digital hologram. The spatial frequencies (u_0,v_0) localize the useful information and they must be adjusted to minimize the overlapping of the three diffraction orders. By applying a bandwidth-limited filter ($\Delta u \times \Delta v$ width) around the spatial frequency (u_0,v_0), and after filtering and inverse two-dimensional (2D) Fourier transform, we get the object complex amplitude:

$$\begin{aligned} O_{+1}(x,y) &= FT^{-1}\left[C_1(u-u_0, v-v_0)\right] \\ &\cong a_r\left\{a_O(x,y)\exp\left[i\phi_O(x,y)\right]\exp\left[2i\pi(u_0 x + v_0 y)\right]\right\} * h(x,y) \end{aligned}, \qquad [1.13]$$

where the symbol * means convolution and $h(x,y)$ is the impulse response corresponding to the filtering applied in the Fourier domain.

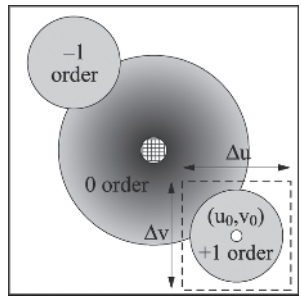

Figure 1.4. *Spectral distribution of orders and spectral filtering*

The impulse response of the filter is such that:

$$h(x,y) = \Delta u \Delta v \exp\left[2i\pi\left(u_0 x + v_0 y\right)\right] \mathrm{sinc}\left(\pi \Delta u x\right) \mathrm{sinc}\left(\pi \Delta v y\right), \quad [1.14]$$

The spatial resolution is then related to $1/\Delta u$ and $1/\Delta v$, respectively, in the x-y axis. In addition, the phase recovered with equation [1.13] includes the spatial carrier modulation that has to be removed. This may be achieved by multiplying O_{+1} by $\exp[-2i\pi(u_0 x + v_0 y)]$.

Note that a filter having a circular bandwidth (instead of a rectangular bandwidth) can also be used [CUC 99a]. In that case, the impulse response of the filter is proportional to a J_0 Bessel function.

Then, the optical object phase at the hologram plane can be estimated from relation:

$$\phi_O(x,y) = \tan^{-1}\left(\frac{\Im_m\left[O_{+1}(x,y)\right]}{\Re_e\left[O_{+1}(x,y)\right]}\right), \quad [1.15]$$

and the object amplitude by:

$$a_O(x,y) = \sqrt{\Im_m^2\left[O_{+1}(x,y)\right] + \Re_e^2\left[O_{+1}(x,y)\right]}, \quad [1.16]$$

In equations [1.15] and [1.16], $\Im_m[...]$ and $\Re_e[...]$, respectively, mean the imaginary and real parts of the complex value.

The main advantage of this approach is its capability of recovering the complex object wave through only one acquisition. Thus, there is no time spent heterodyning or moving mirrors and the influence of vibrations is greatly reduced. However, as the diffraction terms are spatially encoded in the hologram, this one shot capability potentially comes at the cost of usable bandwidth (filter with width $\Delta u \times \Delta v$). In addition, the frequency modulation, induced by the angle between the reference and the object waves, has to guarantee the separation of the information contained in the different diffraction terms that are encoded in the hologram while carrying a frequency compatible with the sampling capacity of digital detectors.

However, in the field of microscopy, the microscope objective usually allows us to properly adapt the object wave field to the sampling capacity of the camera. Definitively, the lateral components of the wave vector $k_{x \text{ or } y}$ are divided by the magnification factor M of the microscope objective. Practically, when a standard camera with pixels at a few microns is used, microscope objective with magnification larger than ×20 makes possible obtaining diffraction-limited resolution even when high numerical apertures (NAs) are considered [MAR 05]. It should also be mentioned that the numerical reconstruction of the object wavefront, particularly its propagation, represents a breakthrough in modern optics and specifically in microscopy [MAR 13]. Indeed, in addition to the possibility to achieve off-line autofocusing [LAN 08, LIE 04a, LIE 04c, DUB 06a] and to extend the depth of focus [FER 05], these numerical reconstruction procedures permit us to mimic complex optical systems as well as to compensate for aberrations [COL 06a, COL 06b], distortions and experimental noise leading to the development of various simplified and robust interferometric configurations able to quantitatively measure optical path lengths with ultrahigh resolution [MAR 13, LEE 13], in practice down to the subnanometer scale [KUH 08], depending on the wavelength and other parameters including the integration time.

1.1.3.2. *Phase-shifting digital holography*

In contrast to off-axis digital holography (Fourier domain), the complex amplitude of the object wave can be directly extracted by

using phase-shifting methods in the temporal domain [CRE 88, DOR 99]. This approach was described by Yamaguchi in 1997 [YAM 97, YAM 01a, YAM 01b] and leads to the reconstruction of an image free from the zero-order and of the twin image (–1 order). Consider the hologram equation written as:

$$H = a_r^{\,2} + a_O^{\,2} + 2a_r a_O \cos\left(\phi_O - \phi_r\right) \qquad [1.17]$$

Basically, in equation [1.17] we should consider three unknowns: the offset term $a_r^2+a_O^2$, the modulation term $2a_ra_O$ and the phase of the cosine function, $\varphi_O-\varphi_r$. So, with at least three values for H, we should be able to solve these three unknowns. This can be done by shifting the phase in the cosine function, by adding in the holographic interferometer a phase modulator. Practically, a piezoelectric transducer (PZT) is used (although other methods do exist) [CRE 88, DOR 99]. The PZT is stamped to a mirror and applying a small voltage to the PZT has to slightly move the mirror as a consequence, and thus to shift the optical phase. With at least three positions of the mirror, the object wave field can be recovered. The robustness of the method increases with increasing the number of phase-shifted holograms. Consider a phase-shifted hologram with a phase-shift being an integer division of 2π, i.e. $2\pi/P$, with P an integer. We have:

$$H_p = a_r^{\,2} + a_O^{\,2} + 2a_r a_O \cos\left(\phi_O - \phi_r + 2\left(p-1\right)\pi / P\right) \qquad [1.18]$$

with $p = 1, 2, \ldots, P$. For $P \geq 3$, the phase of the object wave in the detector plane may be calculated by [GRE 84]:

$$\phi_O = \phi_r + \arctan\left\{\frac{\sum_{n=1}^{P} H_p \sin\left(2\pi\left(p-1\right)/P\right)}{\sum_{n=1}^{P} H_p \cos\left(2\pi\left(p-1\right)/P\right)}\right\} \qquad [1.19]$$

and the amplitude is calculated by:

$$a_O = \frac{1}{2a_r}\sqrt{\left(\sum_{p=1}^{P} H_p \sin\left(2\pi\left(p-1\right)/P\right)\right)^2 + \left(\sum_{p=1}^{P} H_p \cos\left(2\pi\left(p-1\right)/P\right)\right)^2} \qquad [1.20]$$

If the reference wave is plane or spherical, that is free from aberrations, the phase $\phi_O(x,y)$ may be determined without ambiguity and compensated. The complex wave may be evaluated and the object may be directly reconstructed. Using the conjugate complex wave, we may calculate the twin image.

With $P = 4$, we obtain the most widely used method, which was proposed by Yamaguchi and Zhang [YAM 97], using four $\pi/2$ phase-shifted holograms [CRE 88, WYA 75]. In this case, we have:

$$\phi_O = \phi_r + \arctan\left\{\frac{H_4 - H_2}{H_1 - H_3}\right\}$$
$$a_O = \frac{1}{4a_r}\sqrt{\left[H_1 - H_3\right]^2 + \left[H_4 - H_2\right]^2} \qquad [1.21]$$

1.1.3.3. *Parallel phase-shifting*

In the technique of phase-shifting, both the single-shot and real-time capability of digital holography are lost because of the sequential recording of holograms. The four holograms are sequentially recorded by using reference waves with different phase retardations, such as 0, $\pi/2$, π and $3\pi/2$. Although the phase-shifting method achieves noiseless images, it is useless for the instantaneous measurement of moving objects. Even though off-axis digital holography is one candidate for instantaneously obtaining only the first-order diffracted wave, it has some drawbacks: a high-resolution image sensor is required to record spatial carrier fringes and the spatial bandwidth has to be judiciously occupied (see Figure 1.4). In parallel phase-shifting digital holography, the four kinds of phase-shifting are simultaneously carried out for the reference wave in each segment consisting of 2×2 pixels of the image sensor in the recording hologram; thus, it implements four phase-shifting processes by using a spatial division-multiplexing technique. The four holograms required for the phase-shifting interferometry are numerically generated from a hologram recorded with the reference wave. The recording process of the technique is schematically illustrated in Figure 1.5 [AWA 06a, AWA 6b].

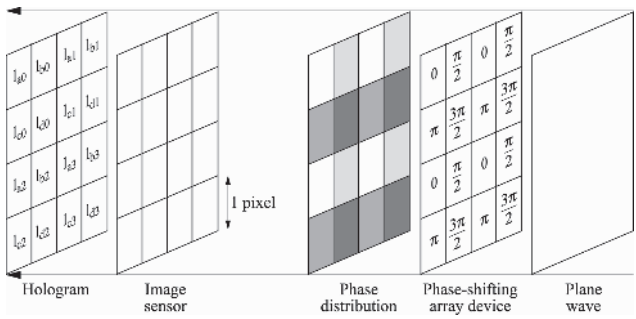

Figure 1.5. *Implementation of parallel phase-shifting digital holography, phase-shifting array device and the distribution of the reference wave for parallel four-step phase-shifting (from [AWA 06a])*

A phase-shifting device array is placed in the reference beam in the holographic interferometer. The array device is a segmented array with a 2 × 2 cell configuration that generates the periodic four-step phase distributions 0, π/2, π and 3π/2. The array device can be implemented by using a glass plate with a periodic four-step thickness. The array device is imaged onto the image sensor so that the phase distribution of the reference wave at the image sensor plane corresponds with the arrangement of pixels in the image sensor. The size of the imaged cells at the image sensor is the same as that of the pixels. Thus, the image sensor captures a hologram recorded with the reference wave containing the four-step phase distributions. The pixels containing the same phase-shift are extracted from the recorded hologram. For each phase-shift, the extracted pixels are relocated in another 2D image at the same addresses at which they were located before being extracted. The values of the pixels not relocated in the 2D image are simply linearly interpolated by using the adjacent pixel values in the reconstruction process. By carrying out this relocation and interpolation for the four phase-shifts, four holograms H_1, H_2, H_3 and H_4 are obtained. Then, the amplitude and phase of the complex object field can be calculated using the conventional algorithm [1.21].

1.1.3.4. *Heterodyne digital holography*

In a heterodyne digital holographic scheme, the reference beam is dynamically phase-shifted with respect to the object field. This shift

produces time-varying interferograms at the sensor plane. Generally, the phase-shift is linear in time (frequency shift). The hologram in the detector plane results from the interference of the object wave with the δf-shifted reference wave, as described in equation [1.22]:

$$\begin{aligned} H &= \left|U_r \exp\left(2i\pi\delta f t\right) + U_O\right|^2 \\ &= \left|U_r\right|^2 + \left|U_O\right|^2 + U_r^* U_O \exp\left(-2i\pi\delta f t\right) + U_r U_O^* \exp\left(+2i\pi\delta f t\right) \end{aligned} \quad . \quad [1.22]$$

A set of P holograms H_p (p = 1, 2,…, P) is recorded within a δf period at $t_p = 2\pi(p-1)/\delta f$ [LE 00, LE 01]. The demodulation algorithm is then:

$$U_O = \frac{1}{P}\frac{1}{U_r^*}\sum_{p=1}^{p=P} H_p \exp\left[\frac{2i\pi\left(p-1\right)}{P}\right]. \quad [1.23]$$

For P = 4, the object complex wave is proportional to $(H_1-H_3)+i(H_2-H_4)$ and the algorithm is quite similar to that provided in equation [1.21]. Thus, heterodyne holography measures the phase, using the information obtained at different times. From the practical point of view, the frequency shift is provided by combining two acousto-optic modulators working at $\Delta f+\delta f$ and Δf, respectively, and δf is adjusted to be equal to one quarter of the sensor frame rate [LE 00, LE 01, ABS 10, SAM 11].

Combining off-axis holography with heterodyning permits us to reach the shot-noise detection and to achieve the ultimate sensitivity of digital holography [ATL 07, ATL 08, GRO 07, GRO 08].

1.2. Back-propagation to the object plane

The previous sections have discussed on the basics of digital hologram recording and demodulation. In order to discuss the digital reconstruction of the object wave at the object plane (and not necessarily at the sensor plane), this section presents the basics of the scalar diffraction of light. Algorithms used to back-propagate the object field estimated at the sensor plane are based on this approach.

1.2.1. *Monochromatic spherical and plane waves*

In this chapter, the time dependence of the optical wavefront is implicit and not included in the equations describing the diffraction. In a space described by a Cartesian coordinate system O*xyz*, a point *P* is described by a set of three coordinates (*x*, *y*, *z*) and we will use the modulus of the distance **OP** by $r = |\mathbf{OP}| = \sqrt{x^2 + y^2 + z^2}$. We also use $k = 2\pi/\lambda$, the modulus of the wave vector, here λ is the wavelength of the light. We assume that the optical field is written as:

$$U(P,t) = U(P)\exp(-2i\pi\nu t) \qquad [1.24]$$

where $U(P)$ is the complex amplitude at the observation point $P(x, y, z)$ and ν is the frequency of the light wave. Let us begin with the definition of a spherical wave. If the point source of a spherical wave is at the origin of a Cartesian coordinate system, the complex amplitude of a spherical wave can, therefore, be expressed by [GOO 72, COL 70, YAR 85]:

$$U(x,y,z) = \begin{cases} \dfrac{A_0}{r}\exp(ikr) & (divergent) \\ \dfrac{A_0}{r}\exp(-ikr) & (convergent) \end{cases} \qquad [1.25]$$

We note that the amplitude is proportional to the inverse of the distance between the point source and *r*, the observation point. When the center of the spherical wave is at point (x_c, y_c, z_c), instead of the origin, the expressions are identical, with *r* substituted for:

$$r = \sqrt{(x-x_c)^2 + (y-y_c)^2 + (z-z_c)^2} \qquad [1.26]$$

For a plane wave propagating in a homogeneous medium, the wavefront is perpendicular to the propagation direction. The plane wave can be written as:

$$U(x,y,z) = A_0 \exp\left[ik(x\cos\alpha + y\cos\beta + z\cos\gamma)\right] \qquad [1.27]$$

The propagation direction is defined by the direction cosines $\cos\alpha$, $\cos\beta$ and $\cos\gamma$ of [1.27]. This relation shows that for a real number C, the expression $x\cos\alpha + y\cos\beta + z\cos\gamma = C$ describes a phase plane whose normal is in the direction given by the cosines $\cos\alpha$, $\cos\beta$ and $\cos\gamma$. Since different values of C correspond to different parallel planes, expression [1.27] represents a wave propagating in the direction normal to these planes.

Figure 1.6 illustrates the concept of spherical and plane waves. Figure 1.6(a) shows a spherical wavefront with center A, that emits a divergent spherical wavefront Σ (see [1.25]). In a homogeneous medium, rays are perpendicular to Σ, and the wave is deformed when propagating to the right (to the left for a convergent wavefront). When the point source tends to infinity, the spherical wave tends to a plane wave, as illustrated in Figure 1.6(b). In this case, the rays become parallel and the beam propagates without any deformation.

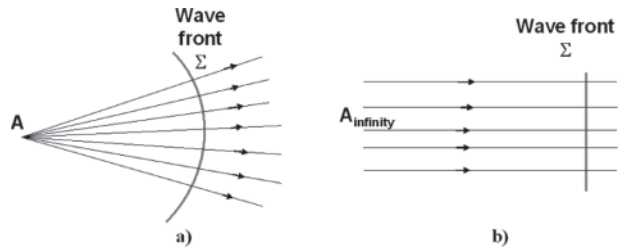

Figure 1.6. *Illustration of spherical and plane waves. For a color version of this figure, see www.iste.co.uk/picart/digiholography.zip*

1.2.2. *Propagation equation*

The wave aspect of light is described by the classical theory of electromagnetism, by the Maxwell's equations [BOR 99, GOO 72, LAU 10, YAR 85]. In this chapter, we consider the case of a homogeneous medium. After some mathematics, Maxwell's equations can be reduced to this propagation equation:

$$\nabla^2 \boldsymbol{E} - \frac{1}{c^2}\frac{\partial^2 \boldsymbol{E}}{\partial t^2} = 0, \qquad [1.28]$$

where **E** is the electric field and c is the velocity of light in the medium. Operator $\nabla^2 = \partial^2/\partial x^2 + \partial^2/\partial y^2 + \partial^2/\partial z^2$ is the Laplacian operator. Note that [1.28] is also valid for the magnetic field **B**.

1.2.3. *Angular spectrum transfer function*

Substituting [1.24] into [1.28], we obtain an equation which is independent of time t, known as the Helmholtz equation:

$$\left(\nabla^2 + k^2\right)U(P) = 0 \qquad [1.29]$$

This equation can be solved in the Fourier domain. We suppose that z is the distance between the initial and observation planes, and that $U(x,y,0)$ and $U(x, y, z)$ are the respective complex amplitudes of these two planes. Moreover, in the frequency space, their spectral functions are $G_0(u,v)$ and $G_z(u,v)$, respectively, (u,v) being the spatial frequencies associated with the spatial coordinates (x, y). These two functions are defined by:

$$G_0(u,v) = \int_{-\infty}^{\infty}\int_{-\infty}^{\infty} U(x,y,0)\exp\left[-2i\pi(ux+vy)\right]dxdy \qquad [1.30]$$

$$G_z(u,v) = \int_{-\infty}^{\infty}\int_{-\infty}^{\infty} U(x,y,z)\exp\left[-2i\pi(ux+vy)\right]dxdy \qquad [1.31]$$

The demonstration will not be provided in this chapter; a general solution to the differential equation can be expressed with the Fourier components of $U(x,y,0)$ and $U(x, y, z)$ according to:

$$G_z(u,v) = G_0(u,v)\exp\left[\frac{2i\pi}{\lambda} z\sqrt{1-(\lambda u)^2-(\lambda v)^2}\right] \qquad [1.32]$$

Then the complex field at distance z can be obtained by:

$$U(x,y,z) = \int_{-\infty}^{\infty}\int_{-\infty}^{\infty} G_z(u,v)\exp\left[2i\pi(ux+vy)\right]dudv \qquad [1.33]$$

So, we have a relation between the spectrum of the wave in the initial plane and that obtain in the observation plane. This relation shows that, in the frequency space, the spectral variation in complex amplitude caused by the propagation of light over the distance z is represented by its multiplication by a phase-delay factor:

$$G(u,v) = \exp\left[2i\pi z / \lambda\sqrt{1-(\lambda u)^2 - (\lambda v)^2} \right] \qquad [1.34]$$

According to the theory of linear systems, the process of diffraction is a transformation of the light field across an optical system, as the phase-delay factor can be interpreted as a transfer function in the frequency space. This interpretation of the propagation of light is called *the propagation of the angular spectrum* and the associated transfer function [1.34] is called *the angular spectrum transfer function*. Figure 1.7 illustrates this approach.

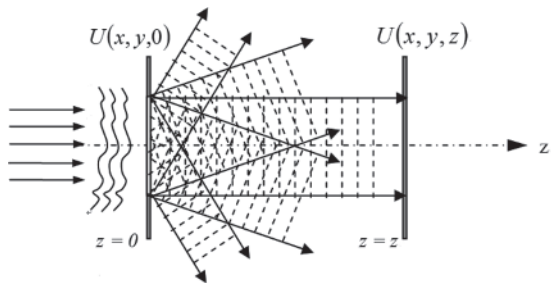

Figure 1.7. *Scheme of the diffraction by the angular spectrum*

Figure 1.7 means that that the field $U(x,y,z)$ can be considered as a superposition of plane waves of amplitude $G_z(u,v)dudv$ propagating in a direction whose cosines are $\{\cos\alpha, \cos\beta, \cos\gamma\} = \left\{\lambda u, \lambda v, \sqrt{1-(\lambda u)^2-(\lambda v)^2}\right\}$. From the diffraction of the angular spectrum, [1.34] means that the elementary waves satisfying $1-(\lambda u)^2-(\lambda v)^2 < 0$ are attenuated by the propagation, i.e. all the components satisfying this relation only exist in a zone very close to the initial plane. These components of the angular spectrum are, therefore, called “evanescent waves”. As the

components of the observation plane must satisfy the relation $1-(\lambda u)^2-(\lambda v)^2>0$, i.e. $u^2+v^2<1/\lambda^2$, propagation in free space can be considered as an ideal low-pass filter of radius $1/\lambda$ in the frequency space. Consequently, on the condition that we can obtain the spectrum of $U(x,y,0)$, the spectrum in the observation plane, $U(x, y, z)$ can be expressed by relation [1.32]. Using the direct and inverse Fourier transforms (FT and FT^{-1}), the diffraction calculation process can be described as:

$$U(x,y,z)=FT^{-1}\left\{FT\{U(x,y,0)\}\exp\left[\frac{2i\pi}{\lambda}z\sqrt{1-(\lambda u)^2-(\lambda v)^2}\right]\right\} \qquad [1.35]$$

1.2.4. *Kirchhoff and Rayleigh–Sommerfeld formulas*

There also exist two more solutions to the Helmholtz equation: Kirchhoff's formula and that of Rayleigh–Sommerfeld. Using the coordinates shown in Figure 1.8 which represents the relationship between the initial plane and the observation plane, these two formulas are written in the same mathematical expression [GOO 05]:

$$U(x,y,d_0)=\frac{1}{i\lambda}\int_{-\infty}^{\infty}\int_{-\infty}^{\infty}U(X,Y,0)\frac{\exp(ikr)}{r}K(\theta)\,dXdY \qquad [1.36]$$

where

$$r=\sqrt{(x-X)^2+(y-Y)^2+d_0^2} \qquad [1.37]$$

and θ is the angle between the normal at point $(X,Y,0)$, and the vector **MP** from point $(X,Y,0)$ to point (x, y, d_0) (see Figure 1.8), $K(\theta)$ is called the obliquity factor and its three different expressions correspond to three different formulations [GOO 05].

- $K(\theta)=\dfrac{\cos\theta+1}{2}$ Kirchhoff's formula;
- $K(\theta)=\cos\theta$ first Rayleigh–Sommerfeld solution;
- $K(\theta)=1$ second Rayleigh–Sommerfeld solution.

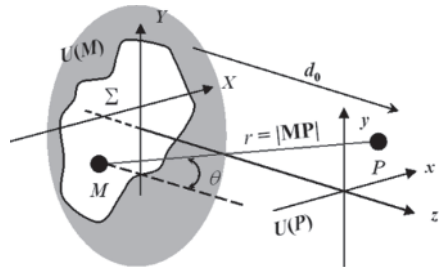

Figure 1.8. *Relation between the initial diffraction plane and the observation plane. For a color version of this figure, see www.iste.co.uk/picart/digiholography.zip*

Even though there exist certain inconsistencies [GOO 05, BOR 99], Kirchhoff's formula gives results in remarkable agreement with experiment, and it is for this reason that it is widely applied in practice. Furthermore, since the angle θ is often small in experimental configurations, the obliquity factors of the three formulations are roughly equal to unity. Thus, the Kirchhoff, Rayleigh–Sommerfeld and angular spectrum formulas are considered as equivalent representations of diffraction. The derivations of the Kirchhoff and Rayleigh–Sommerfeld approaches are presented in detail in [GOO 05]. Readers who would like to go into these aspects in greater detail are invited to familiarize themselves with these appraoches.

1.2.5. *Fresnel approximation and Fresnel diffraction integral*

The equations proposed previously are complex and this is due to the presence of a square root in the complex exponentials. In practice, problems of diffraction quite often concern paraxial propagation, and to simplify the theoretical analysis, we generally use Fresnel's approximation. Let d_0 be the diffraction distance, and expanding the square root in [1.34] to the first order leads to:

$$G(u,v) \cong \exp\left[ikd_0\right]\exp\left[-i\pi\lambda d_0\left(u^2+v^2\right)\right] \qquad [1.38]$$

Given that expression [1.35] can be written in the form of a convolution (* means convolution):

$$U(x,y,d_0) = U(x,y,0) * FT^{-1}\left\{G(u,v)\right\} \qquad [1.39]$$

Substituting [1.38] into [1.39] and knowing that the inverse Fourier transform of $G(u,v)$ is an analytic function, we have:

$$U(x,y,d_0) = U(x,y,0) * \frac{\exp(ikd_0)}{i\lambda d_0} \exp\left[\frac{i\pi}{\lambda d_0}\left(x^2+y^2\right)\right], \quad [1.40]$$

In [1.40], we recognize a convolution of $U(x,y,0)$ with the impulse response of free space propagation that will be denoted as $h(x, y, d_0)$:

$$h(x,y,d_0) = -\frac{i}{\lambda d_0} \exp\left[ikd_0\right] \exp\left[\frac{i\pi}{\lambda d_0}\left(x^2+y^2\right)\right]. \quad [1.41]$$

Equation [1.41] can also be written as:

$$U(x,y,d_0) = \frac{\exp(ikd_0)}{i\lambda d_0} \int_{-\infty}^{\infty}\int_{-\infty}^{\infty} U(X,Y,0) \exp\left\{\frac{i\pi}{\lambda d_0}\left[(x-X)^2+(y-Y)^2\right]\right\} dXdY \quad [1.42]$$

Equation [1.42] constitutes *Fresnel's diffraction integral*. Note that this approximation consists of replacing spherical wavelets (see [1.25]) by quadratic waves (parabolic surface approximation). Developing the quadratic terms in the exponential of [1.42] leads us to:

$$\begin{aligned} U(x,y,d_0) &= \frac{\exp(ikd_0)}{i\lambda d_0} \exp\left[\frac{i\pi}{\lambda d_0}\left(x^2+y^2\right)\right] \times \\ &\int_{-\infty}^{\infty}\int_{-\infty}^{\infty} U(X,Y,0) \exp\left[\frac{i\pi}{\lambda d_0}\left(X^2+Y^2\right)\right] \exp\left[-2i\pi\left(\frac{x}{\lambda d_0}X + \frac{y}{\lambda d_0}Y\right)\right] dXdY \end{aligned} \quad [1.43]$$

Thus, with the exception of multiplicative phase and amplitude factors which are independent of X and Y, we can calculate the function $U(x, y, d_0)$ by carrying out the Fourier transform of:

$$U(X,Y,0) \exp\left[\frac{i\pi}{\lambda d_0}\left(X^2+Y^2\right)\right] \quad [1.44]$$

This transformation must be evaluated at the frequencies $(u,v) = (x/\lambda d_0,\ y/\lambda d_0)$ to guarantee a correct spatial scale in the observation plane. The calculation of the two Fresnel diffraction integrals is relatively simple compared to the formulas which

rigorously satisfy the Helmholtz equation. In the regime of paraxial propagation, this approximation is relatively precise. By defining the Fresnel transfer function [GOO 05] as:

$$G_F(u,v) = \exp\left[\frac{2i\pi z}{\lambda}\right]\exp\left[-i\lambda z\left(u^2+v^2\right)\right] \qquad [1.45]$$

The Fresnel approximation can be expressed by:

$$U(x,y,z) = FT^{-1}\left\{FT\left\{U(x,y,0)\right\}G_F(u,v)\right\} \qquad [1.46]$$

This expression is analogous to the angular spectrum formulation [1.35], but the difference is related to the different transfer functions of the two formulas.

The next section discusses the use of the theoretical basics of wave propagation to numerically reconstruct the object wave at the object plane (which is not necessarily the same as the recording plane).

1.3. Numerical reconstruction of digital holograms

1.3.1. *Discrete Fresnel transform*

1.3.1.1. *Algorithm*

The numerical reconstruction with the discrete Fresnel transform is based on the discrete version of equation [1.43] and considering the input plane as the hologram plane. The spatial sampling in the hologram plane $(X,Y) = (np_x, mp_y)$ where $(m; n) \in (-M/2,+M/2-1;-N/2,+N/2-1)$ has to be taken into account. At any distance d_r from the recording plane, the reconstructed object field can be calculated according to [1.47], in which U_O is the object wave at the sensor plane estimated from the demodulation (see section 1.1.3):

$$\begin{aligned} A_r(x,y,d_r) &= -\frac{i}{\lambda d_r}\exp\left(\frac{2i\pi d_r}{\lambda}\right)\exp\left[\frac{i\pi}{\lambda d_r}\left(x^2+y^2\right)\right] \\ &\times\sum_{l=-L/2}^{l=+L/2}\sum_{k=-K/2}^{k=+K/2} U_O\left(lp_x,kp_y\right)\exp\left[\frac{i\pi}{\lambda d_r}\left(l^2p_x^2+k^2p_y^2\right)\right]\times\exp\left[-\frac{2i\pi}{\lambda d_r}\left(lp_x x+kp_y y\right)\right] \end{aligned} \qquad [1.47]$$

Note that in off-axis holography, the different diffraction terms encoded in the hologram (zero-order wave, real image and virtual image) are propagated in different directions, thus enabling their separation for reconstruction. This means that equation [1.47] can be directly used with an off-axis hologram (replace U_O by H in [1.47]) to calculate the propagated field at distance d_r. In this case, the reconstructed field appears as illustrated in Figure 1.9.

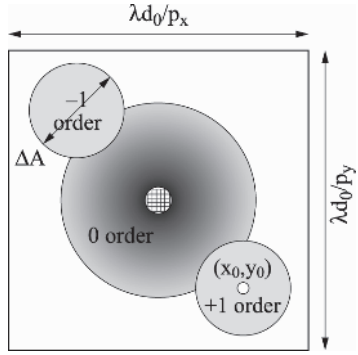

Figure 1.9. *Structure of the reconstructed field of view calculated from an off-axis hologram by using the discrete Fresnel transform*

The spatial localization is related to the spatial carrier frequencies of the hologram, $(x_0, y_0) = (\lambda d_r u_0, \lambda d_r v_0)$, and if the carrier frequencies are correctly adjusted, there is no superposition between the diffractions orders. Then, the object zone can be selected without doubt and the amplitude and phase of the reconstructed object can be estimated.

Since the processor cannot calculate indefinitely, we also have to take into account the spatial sampling in the reconstructed plane. In addition, we can consider that the reconstructed field will be sampled with $(K, L) \geq (M, N)$ pixels. It follows that the sampling pitch is equal to $\Delta\eta = \lambda d_r / L p_x$ and $\Delta\xi = \lambda d_r / K p_y$ [KRE 97, YAM 01a]. The spatial sampling in the image plane is simply $x = l\Delta\eta$ and $y = k\Delta\xi$ with l and k varying from $-L/2$ to $L/2-1$ and from $-K/2$ to $K/2-1$. The schematic diagram of the algorithm is given in Figure 1.10 for a reconstruction distance d_r. This algorithm is known as the single-fast Fourier

transform (S-FFT) algorithm since it uses only a single FFT computation.

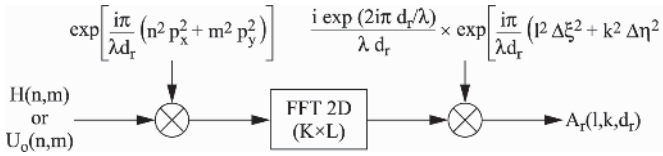

Figure 1.10. *Diagram of the reconstruction with the discrete Fresnel transform*

In addition, the sampling of the quadric phase that is multiplied by the input data (H or U_O) must fulfill the Shannon condition. This means that the minimal distance $d_r^{\min}$ that can be put into the algorithm must fulfill this relation [MAS 03, MAS 99, LI 07]:

$$d_r^{\min} \geq \max\left\{\frac{Np_x^2}{\lambda}, \frac{Mp_y^2}{\lambda}\right\}. \qquad [1.48]$$

Thus, the discrete Fresnel transform cannot be calculated for distance shorter than $d_r^{\min}$.

1.3.1.2. *Spatial resolution in the reconstructed plane*

The computation of the reconstructed field using a finite number of pixels induces a truncate effect. Mathematically, we have to consider the filtering function of the 2D discrete Fourier transform which limits the achievable spatial resolution in the reconstructed plane. It is given by [PIC 08]:

$$\tilde{W}_{NM}(x,y,d_r) = \exp\left[i\pi(N-1)\frac{xp_x}{\lambda d_r} + i\pi(M-1)\frac{yp_y}{\lambda d_r}\right] \times \frac{\sin(\pi Nxp_x/\lambda d_r)}{\sin(\pi xp_x/\lambda d_r)} \frac{\sin(\pi Myp_y/\lambda d_r)}{\sin(\pi yp_y/\lambda d_r)}. \qquad [1.49]$$

This function is periodic and its period can be assimilated to a sinc function [PIC 08]. It is interpreted to be the numerical diffraction pattern of the rectangular aperture constituted by the recorded

hologram. The width of this function gives the *intrinsic spatial resolutions* in the reconstructed plane. They are given by $\rho_x = \lambda d_r/Np_x$ and $\rho_y = \lambda d_r/Mp_y$, respectively, or the x- and y-directions, and they depend on the wavelength, the number of useful sampling pixels and the reconstruction distance.

1.3.1.3. *Effect of defocus and depth of focus*

Although digital holography is not a conventional imaging method, it exhibits some similarities with classical imaging. Especially, the reconstructed images include a depth of focus. The perfect focus is obtained if the spatial resolution reaches its theoretical limits. The contribution to the degradation of the spatial resolution will not be discussed in this section and the readers may have a look at [YAM 01a, PIC 08, PIC 12]. However, to determine the focal depth of the reconstructed image, we can set the width of the defocusing function as having to be approximately equal to ρ_x. If the perfect image distance is d_i, noting $\Delta z = |d_r - d_i|$, the full depth of focus on both sides of the perfect image plane is given by:

$$2\Delta z \cong \frac{2\lambda d_i^2}{N^2 p_x^2} \qquad [1.50]$$

Thus, the focal depth in digital holography is proportional to the square of the angular aperture of the sensor as seen from the object [YAM 01a].

As an illustration, a 2€ coin, 25 mm in diameter, is illuminated at $\lambda = 0.6328$ nm and placed at $d_0 = 660$ mm from the sensor ($N = 1{,}024$, $p_x = 4.65$ µm). The theoretical ideal focused image is obtained with $d_i = -660$ mm and the spatial resolution is $\rho_x = 87.7$ µm in the reconstructed image plane. Then, the depth of focus is estimated at $\Delta z \approx 12.15$ mm. Figure 1.11 provides a set of reconstructed images. Figure 1.11(a) corresponds to the best focus image. Figure 1.11(b) corresponds to an out of focus image with $d_r = d_i - 50$ mm. The image is highly blurred. Figures 1.11(c) and (d) correspond to reconstructions symmetrically included in the depth of focus. As can be seen, the images are focused even if there is a slight difference

between the two images. Figures 1.11(e) and (f) correspond to reconstructions slightly outside the depth of focus. The images become to be blurred by the defocusing [PIC 08], whose width increases with the increase of $|d_r - d_i|$. Figure 1.11 shows that if the reconstruction distance is slightly different from the ideal one, there is no significant difference between reconstructed images.

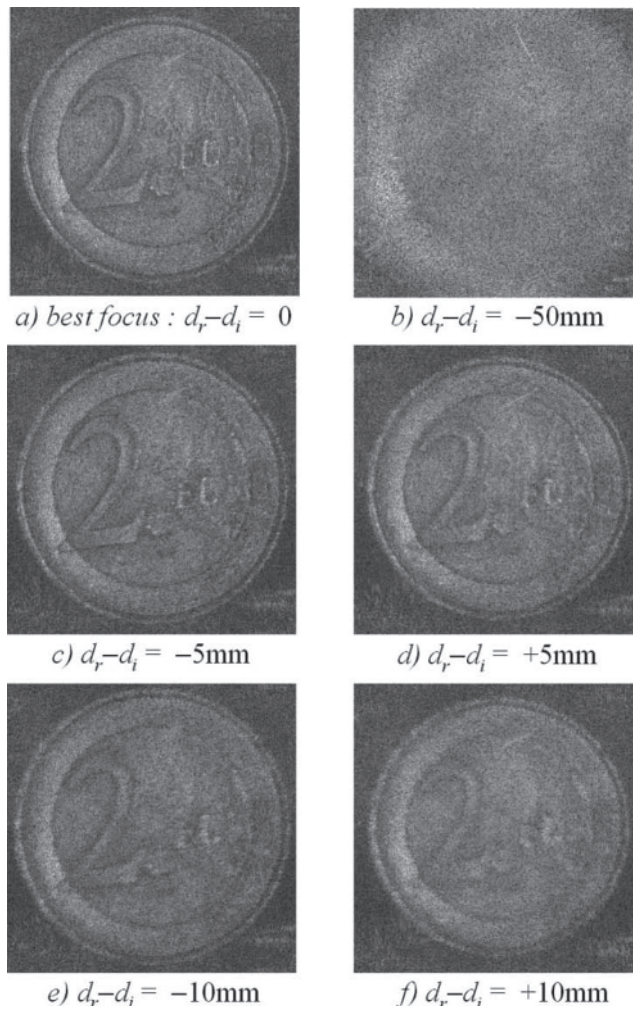

Figure 1.11. *Reconstructed images in and out the depth of focus*

1.3.1.4. *Effect of zero-padding*

Computation of the discrete Fresnel transform with $(K, L) = (N, M)$ uses the data from the raw hologram (H or U_O). If $(K, L) \geq (N, M)$, this case is called "zero-padding" and it consists of adding $(K–N, L–M)$ zeros to the hologram matrix. Fundamentally, these zeros do not add pertinent information; however, they modify the sampling pitches $\Delta\eta = \lambda d_r/Lp_x$ and $\Delta\xi = \lambda d_r/Kp_y$ of the diffracted field. In the case where $(K, L) > (N, M)$, then $\rho_x > \Delta\xi$ and $\rho_y > \Delta\eta$. This means that the intrinsic resolution is not modified because it is imposed by the number of useful pixels (M,N) of the detector area and not by the number of data points of the reconstructed field. However, there is a decrease in the sampling pitch inducing an increase in the "definition" of the image plane. Definitively, this means that we will see more texture in the image: the resolution function will be finely sampled and the granular structure of the object will appear to the observer. Zero-padding of hologram consequently has to make the speckles of the image appear finely but without decreasing their size. This aspect is illustrated in Figure 1.12 in the case of a 2€ coin 25 mm in diameter illuminated at $\lambda = 632.8$ nm which was placed at distance d_0=660 mm from the sensor ($M \times N$ = 1,024 × 1,360 pixels, $p_x = p_y = 4.65$ μm). The number of reconstructed points is chosen to be (512, 1,024, 2,048 and 4,096). When $K = L = 512$ there is a strong reduction of the width of the hologram since the number of data points used for the computation is smaller than the initial matrix. In this case, the intrinsic resolution decreases and the reconstructed image appears very badly. When $K = L = 1{,}024$, the number of data points is approximately equal to that given by the sensor (1,024 against 1,360 in horizontal direction). The image sampling also corresponds approximately to the intrinsic resolution. Thus, the image appears "pixelized". For $K = L =$ 2,048, zero-padding is effective and image sampling is twice as small as intrinsic resolution. So, the resolution function is sampled with a better definition and this facilitates the observation of the fine texture of the image, particularly its speckle. For $K = L = 4{,}096$, image sampling is now four times smaller than the intrinsic resolution. The definition of the image plane is again increased but the speckle does not change its size since it is imposed by the intrinsic resolution (i.e. ρ_x and ρ_y).

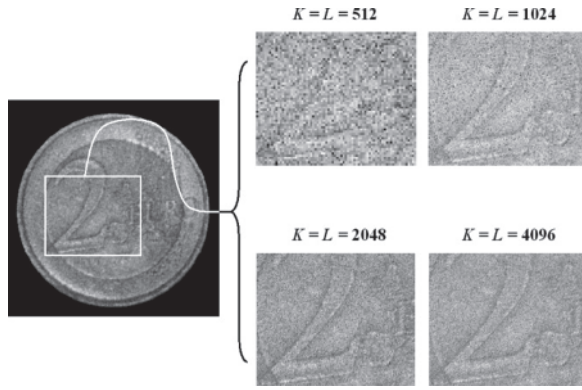

Figure 1.12. *Illustration of the effect of zero-padding*

1.3.2. *Reconstruction with convolution*

1.3.2.1. *Basic algorithm*

The numerical reconstruction with the convolution algorithm is based on the discrete version of equation [1.47] and considering the input plane as the hologram plane. In the same manner as that of the discrete Fresnel transform, the spatial sampling in the hologram plane has to be taken into account. Furthermore, we have to consider the sampling of the angular spectrum transfer function [1.34]. In the Fourier domain calculated by the FFT algorithm, the spatial frequencies are sampled so that $(u,v) = (n\delta u, m\delta v)$, where $(m;n) \in (-M/2,+M/2-1;-N/2,+N/2-1)$ and $(\delta u, \delta v) = (1/Np_x, 1/Mp_y)$.

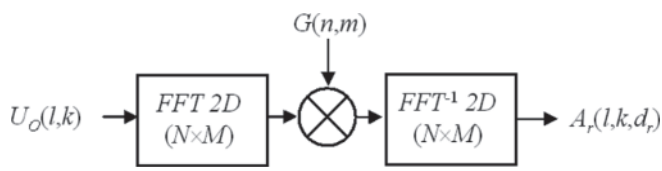

Figure 1.13. *Diagram of the reconstruction with convolution and the angular spectrum transfer function*

At any distance d_r from the recording plane, the reconstructed object field can be calculated according to the algorithm in

Figure 1.13, in which U_O is the object wave at the sensor plane estimated from the demodulation of the hologram (see section 1.1.3). This algorithm is known as the double-fast Fourier transform (D-FFT) algorithm since only two FFTs are required to compute the image plane.

Note that the sampling of the angular spectrum transfer function requires fulfilling the Shannon conditions. The condition is now:

$$d_r^{\max} \leq \min\left\{\frac{Lp_x^2}{\lambda}, \frac{Kp_y^2}{\lambda}\right\}, \qquad [1.51]$$

and is in the opposite way, compared to [1.48]. This means that the angular spectrum transfer function cannot be used to calculate distances larger than $d_r^{\max}$.

In cases of using directly the recorded hologram (i.e. H instead of U_O) as input to the algorithm in Figure 1.13, problems occur that are related to limitation in this approach. This point is discussed in the next section.

1.3.2.2. *Limits of classical approaches of convolution*

A spectral analysis is useful for highlighting the limits of the convolution approach when using directly H as input. From the convolution equation [1.40] and from equation [1.41], the impulse response of free space propagation is a bandwidth-limited function whose spatial bandwidth is related to the finite extent on which it is calculated. Thus, the spatial bandwidth of this convolution kernel is given by:

$$\Delta u_{\text{kernel}} \times \Delta v_{\text{kernel}} = \left(\frac{Np_x}{\lambda \mathrm{d}_r}\right) \times \left(\frac{Mp_y}{\lambda \mathrm{d}_r}\right) \qquad [1.52]$$

Also note that the transfer function of the convolution is a band-pass filter centered at (0,0) spatial frequency. From equation [1.12], the +1 order is localized at spatial frequencies (u_0,v_0). Thus, in order to reconstruct from H, by convolution, the image localized at spatial frequencies (u_0,v_0), we need to check the suitable frequency

localization of the convolution kernel and the object-adapted spatial bandwidth. So as to fully reconstruct the object, the spatial frequency extents of the convolution kernel must be at least that of the object, giving:

$$\Delta u_{\text{kernel}} \times \Delta v_{\text{kernel}} \geq \Delta u_{\text{object}} \times \Delta v_{\text{object}} = \left(\frac{\Delta \mathrm{A}_x}{\lambda \mathrm{d}_r} \right) \times \left(\frac{\Delta \mathrm{A}_y}{\lambda \mathrm{d}_r} \right), \qquad [1.53]$$

where ΔA_x and ΔA_y are, respectively, the object width along the x- and y-directions. Equation [1.53] means that it is not possible to reconstruct directly an object by applying equation [1.47], whose size is larger than the width on which the impulse response is calculated (i.e. $Np_x \times Mp_y$). To increase the spatial frequency bandwidth of the convolution kernel, there are several strategies: (1) zero-padding of the impulse response or the angular spectrum transfer function, (2) design of a filter bank, which consists of a spectral scanning of the object spectrum so as to recover the full bandwidth, and (3) modifying the reconstruction distance so as to naturally increase the spatial bandwidth [PIC 13a]. Approaches 1 and 3 are described in the next two sections.

1.3.2.3. *Zero-padding of the impulse response*

A simple way to increase the spatial frequency bandwidth consists of using the zero-padding of the impulse response or the angular spectrum transfer function to get:

$$\Delta u_{\text{kernel}} = \frac{Lp_x}{\lambda d_r} = \Delta u_{\text{object}} = \frac{\Delta A_x}{\lambda d_r} \qquad [1.54]$$

leading to $L = \Delta A_x / p_x$. So, the number of data points is the ratio between the object size and the pixel pitch of the sensor. The problem linked to the reconstruction of extended objects by using a convolution approach is tantamount to a problem of adaptation of the spatial frequency bandwidth. In order to reconstruct the hologram, the transfer function may be the Fourier transform of the impulse response [1.41] or the angular spectrum transfer function [1.34]. For these options, we must take into account the spectral localization and

the spatial frequency extents of the bandwidth. The zero-padding of the digital hologram with $(K,L)>(M,N)$ leads to extending the horizon for the calculation of the impulse response of the free space propagation, or to an oversampling of the angular transfer function. If the impulse response of free space propagation is used, the spectral localization can be obtained by using the modulation theorem. Centering at frequency (u_0,v_0) is performed by spatially modulating h, according to:

$$h_{\text{kernel}}(x,y,d_r) = h(x,y,d_r) \times \exp\left[+2i\pi\left(u_0 x + v_0 y\right)\right] \qquad [1.55]$$

If the angular spectrum transfer function is used, and as the transfer function must be a band-pass filter in the Fourier domain, we may limit the convolution kernel to the effective spectrum bandwidth and shift G (or G_F) in the spatial frequency space, and set a bandwidth limitation to satisfy sampling requirements. Thus, the associated transfer function becomes:

$$G_{\text{kernel}}(u,v,d_r) = \begin{cases} G(u-u_0, v-v_0, d_r) \\ \qquad \text{if } |u-u_0| \le Lp_x / 2\lambda d_r \text{ and } |v-v_0| \le Kp_y / 2\lambda d_r \\ 0 \qquad \text{elsewhere} \end{cases} \qquad [1.56]$$

As an example, let us consider the numerical reconstruction of the digital hologram of an object sized $\Delta A_x = \Delta A_y = \Delta A = 60$ mm that is recorded with a pixel pitch at $p_x = p_y = 4.65$ µm. Given $L = \Delta A_x / p_x$, we need at least 12,000 × 12,000 data points to reconstruct the full object, which is greater than the calculation capacity of standard personnal computer (PC) computers. So, the approach based on the zero-padding remains limited to object having a "moderate" size, i.e. not too large compared to the sensor width.

1.3.2.4. *Adjustable magnification*

The second method to extend the spatial frequency bandwidth is based on modifying the reconstruction distance. For a given value of $\{K,L\}$, if d_r decreases, then the spatial bandwidth of equation [1.52] increases. The modification of the reconstruction distance can be obtained by using a spherical reconstruction wave, instead of a plane wave as a numerical wave impacting the hologram. This means that

we need to consider H multiplied by a spherical wave $w(x, y, \lambda_c, R_c)$ (equation [1.25]).

The notion of "adjustable magnification" in digital holography requires a brief discussion. In classical holography, the concept of transverse magnification is perceptible since we can easily observe, before our very eyes, the change in the size and position of the diffracted image if we modify the laser wavelength or the curvature of the illuminating beam. However, with a numerical image, this notion is even less obvious. The notion of magnification is related to the field of view (sized $Lp_x \times Kp_y$) that is reconstructed by the convolution. The reconstruction of an extended object, whose physical size $\Delta A_x \times \Delta A_y$ is larger than the field of view, is expected. So that the object may fully appear in the horizon, a transversal magnification $\gamma = \min(Lp_x/\Delta A_x; Kp_y/\Delta A_y)$ must be applied; it is the ratio between the horizon and the object widths. In this way, we may conceive that the adjustable magnification method results in adjusting the reconstructed object size to that of the field of view, which is imposed by calculation capacities or computation speed. Note that several authors proposed algorithms qualified "with adjustable magnification". In 2004, Zhang and Yamaguchi [ZHA 04] proposed an algorithm based on a double Fresnel transform resulting in the adjustment of the side length of the field of view. In 2010, Restrepo and Garcia-Sucerquia [RES 10] discussed the adjustable magnification using the Fresnel–Bluestein transform. Both methods are based on the Fresnel transform (single or double) and the notion of magnification is linked to the ratio between the reconstructed pixel pitch and that of the sensor.

The transverse magnification is related to the ratio between reconstruction and recording distances [LI 09]:

$$\gamma = -\frac{d_r}{d_0}. \qquad [1.57]$$

Thus, the focus on the virtual image is not obtained for $d_r = -d_0$, but for a different distance that depends on the curvature of the recording reference wave and numerical reconstruction wave. This draws the basics of reconstruction with adjustable magnification: a

spherical wave, either a reference or a reconstruction wave [LI 09, TAN 10, PIC 13a], will modify the reconstruction distance, which will modify the spatial frequency bandwidth of convolution, then leading to an adaptation to the object bandwidth. The consequence is that the reconstructed object gets a size which is now compatible with that of the reconstruction field of view. Note that $w(x,y,R_c)$ is also an oscillating function which must fulfill the sampling requirements to be correctly spatially sampled (see equation [1.48]).

The transfer function of convolution can be either the Fourier transform of the impulse response [1.41] or the angular spectrum transfer function (G or G_F) [1.34], [1.45]. For these options, we must take into account the spectral localization and the spatial frequency extents of the bandwidth. Since the transfer function is a band-pass filter in the Fourier domain, we may restrict it to the contour of the object and limit the convolution kernel to the effective object spectrum. Thus, if the object is included in a circular zone ($\Delta A_x = \Delta A_y = \Delta A$), the impulse response can be chosen to be:

$$h_{\text{kernel}}(x,y,d_r) = \begin{cases} h(x,y,d_r) \times \exp\left[+2i\pi\left(u_0 x + v_0 y\right)\right] \\ \qquad \text{if } x^2 + y^2 \le \gamma^2 \Delta A^2 / 4 \\ 0 \quad \text{elsewhere} \end{cases} . \qquad [1.58]$$

Similarly, the impulse response can also be defined for a rectangular object zone [PIC 09]. This restriction of the spatial bandwidth leads to a convolution kernel perfectly adjusted to the object bandwidth. If the angular spectrum transfer function is used, the associated transfer function is thus (circular object):

$$G_{\text{kernel}}(u,v,d_r) = \begin{cases} G\left(u-u_0, v-v_0, d_r\right) \\ \qquad \text{if } \left(u-u_0\right)^2 + \left(v-v_0\right)^2 \le \gamma^2 \Delta A^2 / 4 . \\ 0 \qquad \text{elsewhere} \end{cases} \qquad [1.59]$$

Figure 1.14 shows the diagram for the algorithms based on convolution with adjustable magnification. This algorithm is known as the D-FFT algorithm since it uses two FFT computations

(Figure 1.14(a)) or as the three-fast Fourier transform (T-FFT) computation since it uses three FFT computations (Figure 1.14(b)).

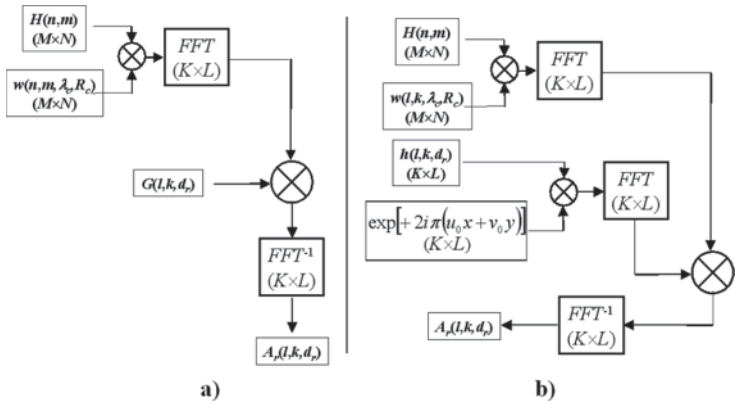

Figure 1.14. *Diagram of the reconstruction with convolution with adjustable magnification: a) with the angular spectrum transfer function and b) with the impulse response of free space propagation*

The use of the adjustable magnification induces a modification in the spatial resolution of the reconstruction process. Since the reconstruction distance changes due to the magnification, the spatial resolutions are:

$$\begin{cases} \rho'_x = \dfrac{\lambda d_r}{N p_x} = \gamma \dfrac{\lambda d_0}{N p_x} = \gamma \rho_x \\ \rho'_y = \dfrac{\lambda d_r}{M p_y} = \gamma \dfrac{\lambda d_0}{M p_y} = \gamma \rho_y \end{cases}, \qquad [1.60]$$

where ρ_x and ρ_y are the spatial resolutions of the holographic process given by the spatial extents of the recording area. From [1.60], the spatial resolution is proportional to the magnification. Since $|\gamma| < 1$ (object larger than sensor), this would mean that the spatial resolution is increased by the process. This is, of course, not physically possible because the numerical process cannot easily transcend the fundamental limits due to diffraction. As indicated previously, the reconstruction process based on adjustable magnification consists of

modifying the object size in the direct space so that it can "enter" the window of the reconstructed field of view. Thus, it is interesting to note that the ratio between the object size and the spatial resolution remains unchanged, either in the direct space or in the reconstructed space. This means that the resolution is not increased in the magnified object. The only effect of the algorithm is on the image "definition", similarly to the effect of zero-padding in the Fresnel transform.

1.4. Holographic setups

This section aims to discuss the different experimental configurations to record a digital hologram. Basic experimental arrangements are provided and few explications on how it works are given.

1.4.1. *Fresnel holography*

The basic setup for digital Fresnel holography is given in Figure 1.15 [SCH 94]. The coherent light from a laser is separated into a reference wave and an object wave. The reference wave is expanded and illuminates directly the sensor, through the 50% beam splitter cube. The object wave, after being expanded, illuminates the object. The object diffracts light to the sensor area. Since the light is coherent, the mixing between the reference and the object waves produces interferences that constitute the digital hologram.

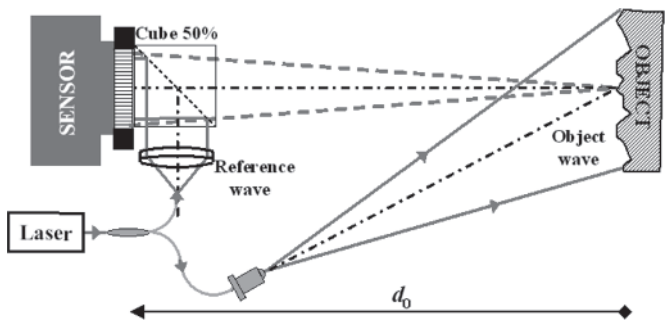

Figure 1.15. *Digital Fresnel holography. For a color version of this figure, see www.iste.co.uk/picart/digiholography.zip*

The numerical reconstruction can be performed with the discrete Fresnel transform in which the reconstruction distance is $d_r = -d_0$ if the reference wave is plane. The hologram can also be reconstructed using the convolution with adjustable magnification, and in this case $d_r \neq -d_0$.

1.4.2. *Fresnel holography with spatial spectrum reduction*

The basic setup is given in Figure 1.16. There are strong similarities with the digital Fresnel holography setup. The use of a diverging lens produces a virtual image of the object, which is smaller and localized closer to the sensor. So, this has for consequence to reduce the size of the setup and to give a more compact setup [SCH 96, MUN 10].

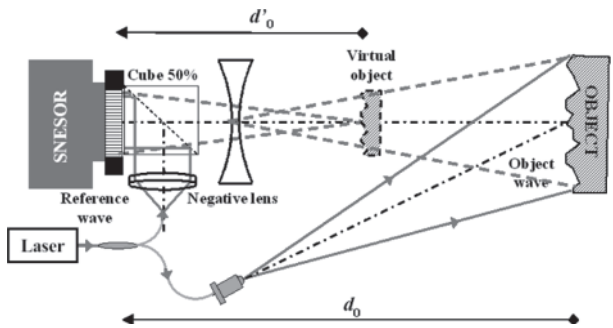

Figure 1.16. *Digital Fresnel holography with reduction of the spatial frequency spectrum. For a color version of this figure, see www.iste.co.uk/picart/digiholography.zip*

The numerical reconstruction can be performed with the discrete Fresnel transform in which the reconstruction distance is $d_r = -d'_0$ if the reference wave is plane. The hologram can also be reconstructed using the convolution with adjustable magnification, and in this case $d_r \neq -d'_0$.

1.4.3. *Fourier holography*

The basic setup is given in Figure 1.17. A convergent lens, with focal distance f', is inserted between the object plane and the sensor

[SEE 01]. The particularity is that the object and the sensor are localized at the focal points of this lens. It follows that the diffracted field at the sensor plane is simply the Fourier transform of the object [GOO 05].

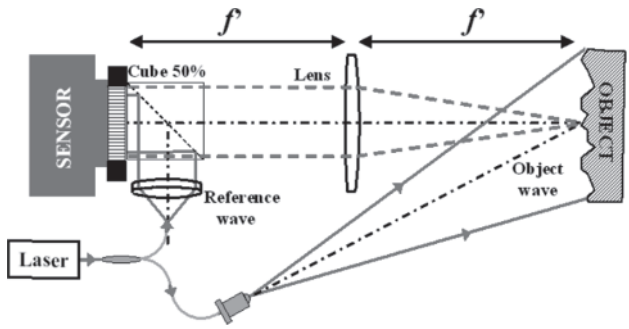

Figure 1.17. *Digital Fourier holography. For a color version of this figure, see www.iste.co.uk/picart/digiholography.zip*

The numerical reconstruction can be performed by computing directly the Fourier transform of the recorded hologram, without multiplying the hologram by the quadratic phase term. The main drawback of this setup is that the sensor and object have to be precisely adjusted at the focal points of the lens. In addition, the hologram of the optical mount can also be recorded in the hologram and this leads to parasitic images in the reconstructed plane.

1.4.4. *Lensless Fourier holography*

So as to simplify the Fourier setup, and to remove the lens, the lensless Fourier setup uses a spherical reference wave instead of a plane one [PED 02, ZHA 08]. The basic setup is given in Figure 1.18. The particularity is that the reference point source is localized in the object plane.

The quadratic terms in the Fresnel integral [1.43] compensate to give directly a Fourier transform. The object field can be reconstructed by calculating the inverse Fourier transform of the recorded hologram, equivalent to $d_r = \infty$ in algorithm of Figure 1.10.

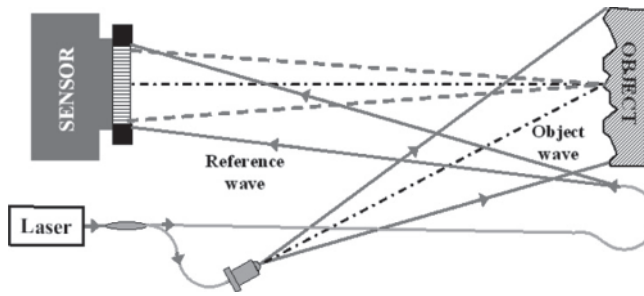

Figure 1.18. *Digital lensless Fourier holography. For a color version of this figure, see www.iste.co.uk/picart/digiholography.zip*

1.4.5. *Image-plane holography*

The basic setup is given in Figure 1.19. Consider an extended object having a size much larger than the recording area; image-plane holography projects the extended object near the sensor area and produces a reduction of the size of the image. A convergent lens, with focal distance *f'*, is inserted between the object plane and the sensor, and it produces the reduced image of the object onto (or nearby) the sensor plane. In such a setup, the influence of the aperture diaphragm (AD) of the lens (AD in Figure 1.19) is significant. It must be pointed out that the recorded hologram is also the *digital Fresnel hologram of the aperture*. This means that the setup must be optimized according to the same rules as those for digital Fresnel holography. So, the NA of the imaging lens must be set to [KAR 12]:

$$\sin\alpha' \le \frac{\lambda}{\left(2+3\sqrt{2}\right)p_x} \qquad [1.61]$$

If this relation is not fulfilled, the three diffraction orders of the hologram of the aperture will overlap. Thus, the useful +1 order of the object will be corrupted by the zero-order of the digital hologram of the aperture. Note that the NA depends only on the wavelength and the pixel pitch, whatever the object size may be, since the optimization of the setup is related to the aperture diameter. In the

case of Fresnel holography, the useful NA of the beam is defined according to that of the sensor-to-object beam. It is equal to $\sin\alpha' \cong \Delta A/2d_0 = \lambda/(2+3\sqrt{2})p_x$ [PIC 08]. It follows that this relation is the same as [1.61]. From this standpoint, the optimization of the optical setup follows the same rules for both methods and does not depend on the object size. That has the consequence of the spatial resolutions of both methods being identical.

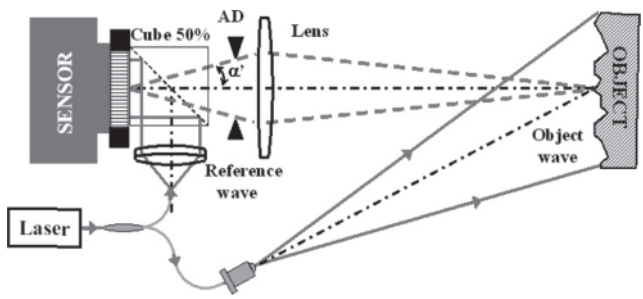

Figure 1.19. *Digital image-plane holography (AD: aperture diaphragm). For a color version of this figure, see www.iste.co.uk/picart/digiholography.zip*

From [1.48], the reconstruction distance d_r must fulfill the sampling condition of the quadratic phase in the discrete Fresnel transform. This means that, *a priori*, the image-plane hologram cannot be computed by the S-FFT method. So, the reconstruction is performed according to the D-FFT strategy with the angular spectrum transfer function, in which $d_r = 0$ when the object is rigorously projected in the recording plane. In the case of perfect image focusing, the transfer function of the convolution kernel tends to a uniform-bandwidth limited function [PED 95].

1.4.6. *Holographic microscopy*

Digital Holographic Microscopy (DHM) is the application of digital holography to microscopy. DHM is distinguished from other methods of microscopy by the fact that it does not require the focused recording of an image projected from the object onto the detector

plane [GAB 49]. The object wave is simply projected by the objective of the microscope toward the detector plane. Since we are recording a digital hologram, we may reconstruct the object with a focus which can be digitally adjusted during the reconstruction process. As the refocusing is performed by digital means, it becomes possible to investigate in three-dimensional (3D) dynamical phenomena, which is actually not possible with usual light microscopy [DUB 06b, DUB 04b, DUB 06c, YOU 14]. There exist other, very similar, techniques of microscopy which differ in name, such as interferential microscopy, optical coherence tomography and diffraction phase microscopy [CUC 99b, DUB 99, DUB 04a, DUB 06b, MAN 05, BHA 12, GIR 13, RAJ 14, FER 06, SHA 10, GAB 12, PAR 12, MAN 08, PIC 13b]. These methods each have in common the use of the coherent combination of an object and a reference wave, allowing the ultimate obtainment of an amplitude image and a phase image of the object. DHM set-ups implemented with spatial partial coherence light sources has permitted to reduce and improve the accuracy of both phase and intensity images [DUB 99, DUB 06b, DUB 04b, DUB 06c, YOU 14]. In traditional microscopy, the image of the object is projected onto the detector, and since there is no reference wave, the essential phase information is lost. DHM facilitates getting what is known as “quantitative phase microscopy” [CHA 07, CHA 06a, CUC 00, CUC 99a, CUC 99b, FER 06, MAN 05, ZHA 98].

Principally, there exist two architectures: using transmission and using reflection. Figure 1.20 describes the basic scheme, without detailing the transmission or reflection configurations. The objective is represented by its lens assembly and AD. In the transmission configuration, the object is illuminated by a collimated beam, and diffracts the light toward the aperture cone of the microscope objective. In the reflection configuration, the object is illuminated by a collimated beam which first passes through the microscope objective, and then diffracts/reflects the light toward the aperture cone of the microscope objective. The light, therefore, crosses the microscope objective twice. Compared to image-plane holography, the configuration is slightly different since we aim at imaging microscopic or nanometric objects.

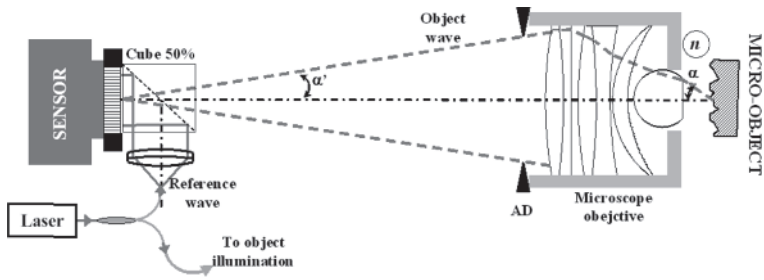

Figure 1.20. *Digital holographic microscopy. For a color version of this figure, see www.iste.co.uk/picart/digiholography.zip*

The image of the object near the sensor plane is produced by the microscope objective having a magnification $|\gamma_{opt}|>>1$ and a high NA $n\sin\alpha$. The holographic microscope has to be optimized similarly to image-plane holography. From the Abbe sinus relation and from [1.61], we have now the condition:

$$n\sin\alpha \le \frac{\left|\gamma_{opt}\right|\lambda}{\left(2+3\sqrt{2}\right)p_x}. \qquad [1.62]$$

With pixels at a few microns and magnification larger than × 20, this relation is always fulfilled.

From [1.48], the reconstruction distance d_r must fulfill the sampling condition of the quadratic phase in the discrete Fresnel transform. This means that, as for image-plane holography, the processing cannot be carried out by the S-FFT method. The reconstruction is performed according to the D-FFT strategy with the angular spectrum transfer function.

1.4.7. *In-line Gabor holography*

In-line Gabor holography refers to the pioneering works of Gabor [GAB 48], who was studying an optical method to compensate for the aberrations in electron microscopy. The setup is quite simple and given in Figure 1.21. The laser beam is expanded and collimated to

produce a parallel beam. It directly illuminates the sensor plane, and this beam constitutes the reference beam. In the path of the beam, an object diffracting light is inserted. This object can be opaque or slightly absorbing. Microscopy of phase objects [GAR 06a, GAR 06b] is also possible. In-line holography is well suited to particle field extraction [ONU 92, HIN 02] and to analyze their statistical size distribution [MAL 04, DEN 06], localization [COE 02, SIN 10] or 3D movement [HIN 02, VER 10].

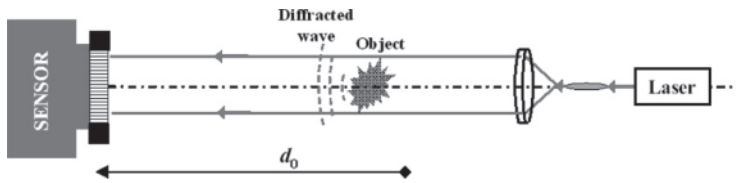

Figure 1.21. *Digital in-line Gabor holography. For a color version of this figure, see www.iste.co.uk/picart/digiholography.zip*

The modeling of the recorded hologram was provided by Onural [ONU 92, ONU 93]. The object distribution is denoted as $s(x,y)$ and the field emerging from the diffracting object plane when it is illuminated by a reference plane wave is denoted as $1-s(x,y)$. In-line holography generally considers that $s(x,y)<<1$. If the object distribution takes only real values, the in-line hologram can be approximately written as:

$$H(x,y) = 1 - s(x,y) * g_z(x,y), \qquad [1.63]$$

with g_z being given by:

$$g_z(x,y) = \frac{2}{\lambda z}\sin\left(\frac{\pi}{\lambda z}\left(x^2+y^2\right)\right). \qquad [1.64]$$

The reconstruction of the hologram can be performed using the discrete Fresnel transform, under the condition that the reconstruction distance is fulfilling equation [1.48], or with the fractional Fourier transform [COE 02]. The latter approach will not be detailed in this chapter (see Chapter 2).

Note that in-line holography, in its basic configuration, suffers from the overlapping of the twin image and zero-order, since there is no independent reference beam to produce a separation of the three orders. The use of spatial light modulator in the optical bath is a key to recover both the amplitude and phase in digital in-line holography [PIC 13b].

1.5. Digital holographic interferometry

Digital holographic interferometry exploits not only the amplitude of the object, but also its phase. This section presents the basic principle of digital holographic interferometry.

1.5.1. *Reconstruction of the phase of the object*

The result of the digital calculation of the diffracted field gives access to the complex amplitude sampled across a mesh corresponding to the number of reconstruction points of the algorithm. From this complex amplitude, we may access two quantities: the amplitude image (modulus) and the phase image (the argument of the field).The object phase, ψ_r, is obtained from:

$$\psi_r = \arg\{A_r\} = \tan^{-1}\left\{\frac{\Im m[A_r]}{\Re e[A_r]}\right\} \mod(2\pi) \qquad [1.65]$$

The phase of the field is calculated using the arctangent function, and as a consequence, the result will be contained within the interval $[-\pi,+\pi]$, i.e. modulo 2π. This phase is random in most of the cases as it is related to the roughness of the object's surface. The reconstructed object is, therefore, marred with speckles [DAI 84]. The estimation of the optical phase of the reconstructed field is key to a large number of applications in digital holography. Note that the phase is relative to an unknown constant. Thus, the absolute phase cannot be obtained with a single wavelength. For the same reason, the notion of relief in digital holography is very different from that in analog holography. Several authors consider that digital holography, using a single hologram, as only reconstructing a "2.5D" volume [KOU 07a].

1.5.2. *Optical phase variations and the sensitivity vector*

Non-contact measurements using holographic methods are based on the variation of the optical phase of the reconstructed object when it is subjected to a stress. This stress may be of a biological, electronic, pneumatic, thermal, acoustic or mechanical nature. When subjected to a stress of any kind, the object is deformed, and thus the optical path along the *source-object-hologram* trajectory will vary. Let us imagine a point A at the light source and a point B attached to the object. When the object is slightly deformed by a stress, point B attached to the object undergoes a 3D change, the displacement vector $\mathbf{D}(D_x, D_y, D_z)$ which generates variations in the optical path from A to B and from B to C (Figure 1.22). These variations are much smaller than the absolute values of these path lengths, and have modules on the order of tens or hundreds of wavelengths of the used light. We denote by $\mathbf{K_e}$ the "illumination" vector of the object, by $\mathbf{K_o}$ the "observation" vector of the object and by n the refractive index around the object. The variation of optical path length is [KRE 96]:

$$\delta_{\text{opt}}(\text{ABC}) = n\mathbf{K_e}.\mathbf{D} - n\mathbf{K_o}.\mathbf{D} = n\mathbf{D}.(\mathbf{K_e} - \mathbf{K_o}) \qquad [1.66]$$

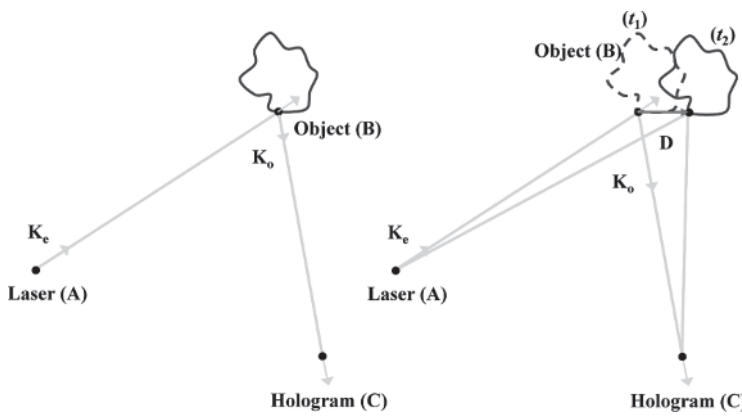

Figure 1.22. *Variation of the source-object-hologram path length. For a color version of this figure, see www.iste.co.uk/picart/digiholography.zip*

The observation vector is related to the direction of observation from the object toward the hologram. The illumination vector represents the direction of illumination of the studied object. We pose:

$$\mathbf{S} = \mathbf{K}_{\mathbf{e}} - \mathbf{K}_{\mathbf{o}} \qquad [1.67]$$

This vector is called the *sensitivity vector*. The sensitivity vector corresponds to the difference between the illumination and observation vectors of the object. The sensitivity vector indicates the displacement direction in which the sensitivity of the apparatus is optimal. Knowledge of the coordinates of this vector is essential for the precise analysis of the amplitude of the displacements. The variation in optical phase induced by the variation in *source-object-hologram* optical path length is, therefore, given by the following relation [KRE 96]:

$$\Delta\phi = \frac{2\pi}{\lambda}\delta_{\text{opt}}(\text{ABC}) = \frac{2n\pi}{\lambda}\mathbf{D}.(\mathbf{K}_{\mathbf{e}} - \mathbf{K}_{\mathbf{o}}) \qquad [1.68]$$

When the object is displaced along the displacement vector **D**, this leads to a variation of the phase, which is itself due to the variation in optical path.

1.5.3. *Phase difference method*

The measurement of the optical phase variations generated by the object requires the recording and reconstruction of at least two holograms (double exposure principle). The first corresponds to a reference hologram, and the second corresponds to a hologram of the object having been subjected to the change. Consequently, the phase variation may be evaluated by calculating the difference in optical phase between the two holograms. Let ψ_{r1} and ψ_{r2} be the optical phases of the first and second hologram, respectively. We then have:

$$\Delta\phi = \psi_{r2} - \psi_{r1} \mod(2\pi) \qquad [1.69]$$

This phase variation will produce digital interference fringes, modulo 2π, which let us quantify the modification of the object

between the two states. The variation in optical path seen in holographic interferometry, therefore, corresponds to the variation in position of the object projected onto the sensitivity vector. We note that for a large number of applications, the refractive index of the medium in which the studied object is placed often equals 1 (air), except for DHM in which cells may be living specimen.

As an illustration, Figure 1.23 shows two phases ψ_{r1} and ψ_{r2} of the first and second holograms, respectively, as well as the phase difference calculated modulo 2π. The two phases are random and uniformly distributed across $[-\pi,+\pi]$. The phase difference is also obtained in $[-\pi,+\pi]$. The case is that of a rough object surface. We observe digital interference fringes which represent phase jumps each time that $\Delta\varphi$ passes $-\pi$ or $+\pi$. We also observe that the result is noisy, which is translated by the appearance of a "salt-and-pepper" texture in the image. This noise is due to the decorrelation of the speckle pattern which exists more or less for each movement of the object [DAI 84, KAR 12].

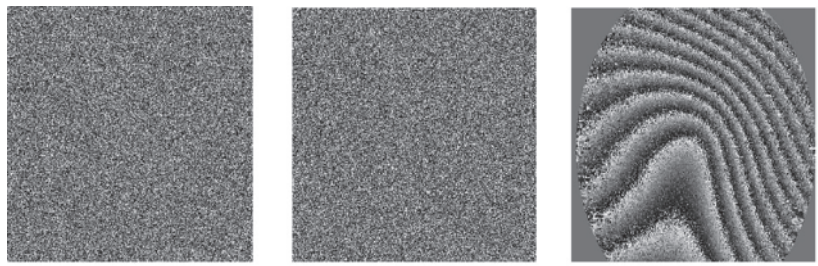

Figure 1.23. *Illustration of the phase-subtraction method*

Such results lead to two conclusions: it is necessary to spatially filter the result to reduce the level of noise (not discussed here) [AEB 99], and, it is necessary to reconstruct the continuity of the phase variation, which is destroyed by calculation using the arctangent function.

1.5.4. *Phase unwrapping*

This operation consists of reconstructing the physical continuity of the phase map. Of course, this continuity may only be reconstructed to within a phase constant, unless we know at which points of the mapping the phase is strictly zero. Figure 1.24 presents an illustration of this operation on one line of a result obtained after the subtraction of two phases.

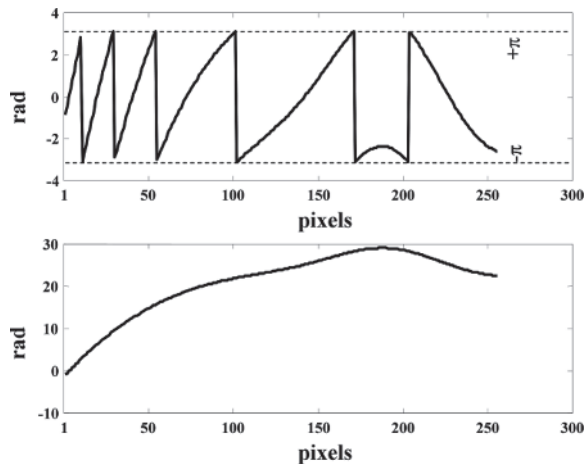

Figure 1.24. *Illustration of the "unwrapping" procedure*

The unwrapping algorithm starts at pixel N°1, and then searches for the phase jumps; at each one detected, -2π or $+2\pi$, it adds $+2\pi$, or -2π so that the phase of two neighboring points is continuous. Phase unwrapping techniques have become more sophisticated in recent years with the appearance of powerful algorithms whose implementation is not always straightforward. For a complete description, the readers should refer to [GHI 98].

1.6. Quantitative phase tomography

In general, a single wavefront determination obtained from a single hologram does not suffice to obtain a full 3D image of an object

[MAR 13]. An exception concerns sparse media, similar to those found in particle image velocimetry (PIV) where each particle can be considered as an isolated punctual object and its position determined in 3D by the methods of in-line holography. In this case, we can resort to sparse image representations to image the cloud of particles in 3D [LIE 04b, LIE 04c, DIX 11]. We must, however, admit that generally the true 3D shape of a given specimen cannot be derived from a single measurement obtained at one wavelength [SHE 10, KOU 07b]. The combination of data reconstructed from several holograms, obtained at either several wavelengths [YU 05] or at several incidence angles (multi-*k*), is needed to achieve true 3D imaging. Several articles report results obtained by changing the wavelength (variable *k*-vector amplitude) as shown, for example, by Marron [MAR 93]. However, in this study, the range of wavelength scan remains very small, and consequently the resolution is weak. Arons *et al.* using Fourier synthesis holography [ARO 96] have also discussed a similar approach. In digital holography, multiple wavelengths have been used to reconstruct 3D structures [KIM 99].

In the field of microscopy, this tomographic imaging technique, based on reconstruction from multiple holograms, has yielded very accurate images of cells, erythrocytes in particular [KUH 09, MON 06]. An alternative, but somehow similar approach, is to use a wide bandwidth source and form a hologram in the plane where the mutual coherence between the object and reference waves is non-zero: this concept introduces coherence gating in the space domain. It has proved to perform well [CUC 97, MAS 05].

The approach consisting of varying the angle of the illumination waves (variable *k*-vector direction) can be used in conjunction with the previous technique where the wavelength is changed (variable *k*-vector amplitude). This angular approach more exactly meets the concept found in the literature under the name of “diffraction tomography” [WOL 69] for reconstruction of the scattering potential associated with the structure of the diffracting object. A diffracted wave can be collected and reconstructed from the holograms at various incidences. The complex amplitude of the measured scattered field is linked to the object function via their Fourier transforms. In

microscopy, a tomographic approach, not based on holography, was presented by Lauer [LAU 02]. A simple way to reconstruct the scattered wave can be based on digital holography: the phase and amplitude of the diffracted wave are directly reconstructed from the hologram and can be used to compute the scattering potential at every point of the specimen.

The scalar approximation has been shown to give good results. However, note that under the first Born approximation [WOL 69], the reconstruction is strictly valid for a low-phase change only, which is proportional to both the object refractive index and size, while under the Rytov approximation, "the size of the object is not a factor" (from [SLA 84]) and therefore the Rytov approximation is expected to give better results for larger objects.

Noting the wave vector of the diffracted wave k_d, k_i that for the illumination wave, and k_O that for the object field, these quantities are linked by the following equation:

$$k_d = k_i + k_O \qquad [1.70]$$

When considering a transmission geometry and only one direction of illumination (only one k_i), only one half of the Ewald sphere could be recorded at best. Moreover, this half-sphere is restricted to a cap of sphere only, because of the limited NA of the microscope objective (NA) used in the holographic scheme (see Figure 1.20). As shown in Figure 1.25(a), a very limited subset of the diffracted wave vectors can be measured. From [1.70], for a given incident direction k_i, and an observation direction k_d, the corresponding wave vector of the object field is $k_O = k_d - k_i$. The set of wave vectors $k_d - k_i$ which are recorded is shown as a bold arc of circle in Figure 1.25(a). The recorded spatial frequency space can be filled using successive variable directions of illumination, leading to recording a more complete subset of the 3D frequency representation of the object, in order to perform a more accurate reconstruction of the object [DEB 08]. The use of tilted illuminating wave permits to record higher frequencies from the Fourier transform of the object field. Figure 1.25(b) illustrates the mapping of the *k*-space with the set of wave vectors of Figure 1.25(a).

Each circle represents the spatial bandwidth available from the holographic setup for each illumination vector. Figure 1.25(c) shows that after scanning the incident vector, a portion of the *k*-space is covered by the measured data. When a large number of incidences angles are scanned, the area covered by the measured wave vectors in the *x*-*y* plane becomes a disk (Figure 1.25(d)).

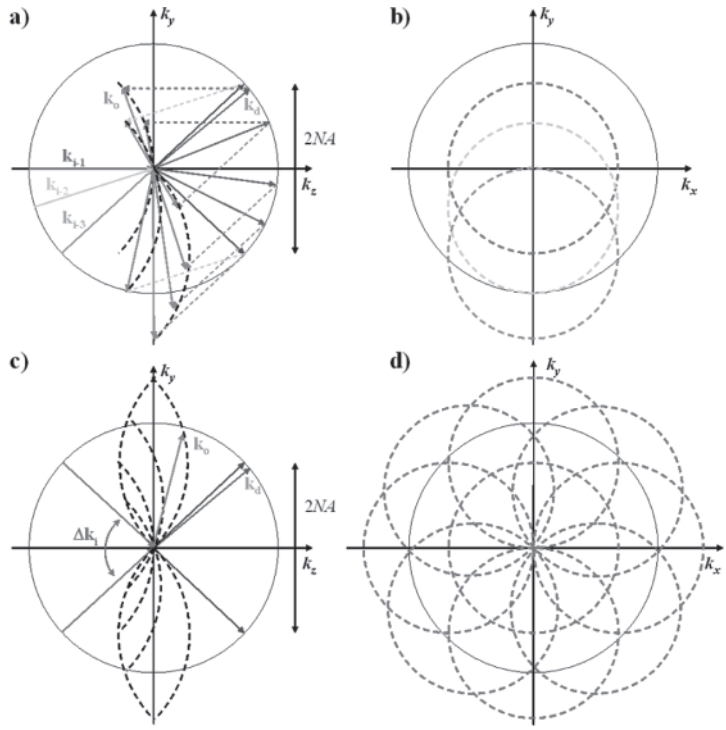

Figure 1.25. *Principle of diffractive tomography: construction of the measured spatial frequency support in the case of transmission (refer to text). For a color version of this figure, see www.iste.co.uk/picart/digiholography.zip*

From these data, the 3D distribution of the refractive index can be established providing, therefore, a 3D tomographic image of the cell constituents.

Tomography of cells based on DHM is new and original. In 2006, a first approach consisting of the rotation of the specimen has been

developed [CHA 06b, CHA 06c]. It was demonstrated that the refractive index of the cell body could be measured in 3D with a spatial resolution better than 3 μm in all directions. Other approaches consisting of rotating the beam rather than the object have been proposed [DEB 09, CHO 07, SUN 09, KIM 11, COT 11]. Kou [KOU 07b] and Sheppard [SHE 10] have compared both approaches in their principles and shown consistent differences in the performance of each modality. In this case, the approach is commonly described as "synthetic aperture imaging" because the effective aperture results from the stitching of several loci (Ewald spheres) in the Fourier domain corresponding to various illuminating directions.

1.7. Conclusion

In this chapter, we have introduced the principles of digital holography, as well as the associated reconstruction methods. Some demodulation techniques of eliminating the zero-order and twin image, to increase the spatial resolution of reconstructed images, have been discussed. The discrete Fresnel transform is the simplest and the most direct calculation method, on the condition that the sampling theorem is respected in the plane of the hologram. This method is certainly the most widely used method, even though it does not guarantee the invariance of the reconstructed horizon with the wavelength [FER 04]. We have presented the methods based on convolution, especially the adjustable-magnification approach which leads to the adaptation of the reconstructed image size to the size of the field of view.

Note that other reconstruction methods based on wavelets are also discussed in the literature. For example, the readers could have a look at [ONU 93, LIE 03, LIE 04a] and [LIE 04b].

We have introduced the methods of holographic interferometry for which the phase of the reconstructed field is the principal parameter. The exploitation of the phase gives versatility to digital holography: quantitative microscopy, phase contrast, profilometry, the measurement of displacement fields, vibrations and fluid mechanics.

Quantitative phase tomography has been introduced and applications are detailed in Chapter 5.

This chapter serves as a basis for the next chapters that will go into advanced holographic methods more thoroughly.

1.8. Bibliography

[ABS 10] ABSIL E., TESSIER G., GROSS M., *et al.*, "Photothermal heterodyne holography of gold nanoparticles", *Optics Express*, vol. 18, pp. 780–786, 2010.

[AEB 99] AEBISCHER H.A., WALDNER S., "A simple and effective method for filtering speckle-interferometric phase fringe patterns", *Optics Communications*, vol. 162, pp. 205–210, 1999.

[ATL 07] ATLAN M., GROSS M., ABSIL E., "Accurate phase-shifting digital interferometry", *Optics Letters*, vol. 32, pp. 1456–1458, 2007.

[ATL 08] ATLAN M., GROSS M., DESBIOLLES P., *et al.*, "Heterodyne holographic microscopy of gold particles", *Optics Letters*, vol. 33, pp. 500–502, 2008.

[ARO 96] ARONS E., DILWORTH D., "Lensless imaging by spatial Fourier synthesis holography", *Applied Optics*, vol. 35, pp. 777–781, 1996.

[AWA 06a] AWATSUJI Y., FUJII A., KUBOTA T., *et al.*, "Parallel three-step phase-shifting digital holography", *Applied Optics*, vol. 45, pp. 2995–3002, 2006.

[AWA 06b] AWATSUJI Y., SASADA M., FUJII A., *et al.*, "Scheme to improve the reconstructed image in parallel quasi-phase-shifting digital holography", *Applied Optics*, vol. 45, pp. 968–974, 2006.

[BHA 12] BHADURI B., PHAM H., MIR M., *et al.*, "Diffraction phase microscopy with white light", *Optics Letters*, vol. 37, pp. 1094–1096, 2012.

[BOR 99] BORN M., WOLF E., *Principles of Optics*, 7th ed., Cambridge University Press, 1999.

[CHA 06a] CHARRIÈRE F., KÜHN J., COLOMB T., *et al.*, "Characterisation of micro lens by digital holographic microscopy", *Applied Optics*, vol. 45, pp. 829–835, 2006.

[CHA 06b] CHARRIÈRE F., MARIAN A., MONTFORT F., *et al.*, "Cell refractive index tomography by digital holographic microscopy", *Optics Letters*, vol. 31, pp. 178–180, 2006.

[CHA 06c] CHARRIÈRE F., PAVILLON N., COLOMB T., *et al.*, "Living specimen tomography by digital holographic microscopy: morphometry of testate amoeba", *Optics Express*, vol. 14, pp. 7005–7013, 2006.

[CHA 07] CHALUT K., BROWN W., WAX A., "Quantitative phase microscopy with asynchronous digital holography", *Optics Express*, vol. 15, pp. 3047–3052, 2007.

[CHO 07] CHOI W., FANG-YEN C., BADIZADEGAN K., *et al.*, "Tomographic phase microscopy", *Nature Methods*, vol. 4, pp. 717–719, 2007.

[COE 02] COETMELLEC S., LEBRUN D., OSKUL C., "Application of the two-dimensional fractional-order Fourier transformation to particle field digital holography", *Journal of the Optical Society of America A*, vol. 19, pp. 1537–1546, 2002.

[COL 70] COLLINS S.A., "Laser-system diffraction integral written in terms of matrix optics", *Journal of the Optical Society of America*, vol. 60, p. 1168, 1970.

[COL 06a] COLOMB T., MONTFORT F., KÜHN J., *et al.*, "Numerical parametric lens for shifting, magnification and complete aberration compensation in digital holographic microscopy", *Journal of the Optical Society of America A,* vol. 23, pp. 3177–3190, 2006.

[COL 06b] COLOMB T., CUCHE E., CHARRIÈRE F., *et al.*, "Automatic procedure for aberration compensation in digital holographic microscopy and applications to specimen shape compensation", *Applied Optics*, vol. 45, pp. 851–863, 2006.

[COQ 95] COQUOZ O., CONDE R., TALEBLOU F., *et al.*, "Performances of endoscopic holography with a multicore optical-fiber", *Applied Optics*, vol. 34, pp. 7186–7193, 1995.

[COT 11] COTTE Y., TOY M.F., DEPEURSINGE C., "Beyond the lateral resolution limit by phase imaging", *Journal of Biomedical Optics*, vol. 16, p. 106007, 2011.

[CRE 88] CREATH K., "Phase measurement interferometry techniques", in WOLF E. (ed.), *Progress in Optics*, North-Holland publishing Company, vol. 26, pp. 349–393, 1988.

[CUC 97] CUCHE E., POSCIO P., DEPEURSINGE C., "Optical tomography by means of a numerical low-coherence holographic technique", *Journal of Optics-Nouvelle Revue d'Optique*, vol. 28, pp. 260–264, 1997.

[CUC 99a] CUCHE E., MARQUET P., DEPEURSINGE C., "Simultaneous amplitude-contrast and quantitative phase-contrast microscopy by numerical reconstruction of Fresnel off-axis holograms", *Applied Optics*, vol. 38, pp. 6994–7001, 1999.

[CUC 99b] CUCHE E., BEVILACQUA F., DEPEURSINGE C., "Digital holography for quantitative phase contrast imaging", *Optics Letters*, vol. 24, pp. 291–293, 1999.

[CUC 00] CUCHE E., MARQUET P., DEPEURSINGE C., "Spatial filtering for zero-order and twin-image elimination in digital off-axis holography", *Applied Optics*, vol. 39, pp. 4070–7075, 2000.

[DAI 84] DAINTY J.C., *Laser Speckle and Related Phenomena*, Springer-Verlag, Berlin, 1984.

[DEB 08] DEBAILLEUL M., SIMON B., GEORGES V., *et al.*, "Holographic microscopy and diffractive microtomography of transparent samples", *Measurement Science and Technology*, vol. 19, pp. 074009–074016, 2008.

[DEB 09] DEBAILLEUL M., GEORGES V., SIMON B., *et al.*, "High-resolution three-dimensional tomographic diffractive microscopy of transparent inorganic and biological samples", *Optics Letters*, vol. 34, pp. 79–81, 2009.

[DEM 03] DEMOLI N., VUKICEVIC D., TORZYNSKI M., "Dynamic digital holographic interferometry with three wavelengths", *Optics Express*, vol. 11, pp. 767–774, 2003.

[DEN 06] DENIS L., FOURNIER C., FOURNEL T., *et al.*, "Direct extraction of the mean particle size from a digital hologram", *Applied Optics*, vol. 45, pp. 944–952, 2006.

[DES 08] DESSE J.M., PICART P., TANKAM P., "Digital three-color holographic interferometry for flow analysis", *Optics Express*, vol. 16, pp. 5471–5480, 2008.

[DES 11] DESSE J.M., PICART P., TANKAM P., "Sensor influence in digital 3λ holographic interferometry", *Measurement Science and Technology*, vol. 22, p. 064005, 2011.

[DES 12] DESSE J.M., PICART P., TANKAM P., "Digital color holography applied to fluid mechanics and structure mechanics", *Optics and Lasers in Engineering*, vol. 50, pp. 18–28, 2012.

[DIX 11] DIXON L., CHEONG F.C., GRIER D.G., "Holographic deconvolution microscopy for high-resolution particle tracking", *Optics Express*, vol. 19, pp. 16410–16417, 2011.

[DOR 99] DORRIO B.V., FERNANDEZ J.L., "Phase evaluation methods in whole-field optical measurement techniques", *Measurement Science and Technology*, vol. 10, pp. 33–55, 1999.

[DUB 99] DUBOIS F., JOANNES L., LEGROS J.C., "Improved three-dimensional imaging with a digital holography microscope with a source of partial spatial coherence", *Applied Optics*, vol. 38, pp. 7085–7094, 1999.

[DUB 04a] DUBOIS F., YOURASSOWSKY C., MONNOM O., "Microscopie en holographie digitale avec une source partiellement cohérente", in FAUPEL M., SMIGIELSKI P., GRZYMALA R. (eds.), *Imagerie et Photonique pour les sciences du vivant et la médecine*, Fontis Media, Fomartis, pp. 287–302, 2004.

[DUB 04b] DUBOIS F., REQUENA M.-L.N., MINETTI C., *et al.*, "Partial spatial coherence effects in digital holographic microscopy with a laser source", *Applied Optics*, vol. 43, pp. 1131–1139, 2004.

[DUB 06a] DUBOIS F., SCHOCKAERT C., CALLENS N., *et al.*, "Focus plane detection criteria in digital holography microscopy by amplitude analysis", *Optics Express*, vol. 14, pp. 5895–5908, 2006.

[DUB 06b] DUBOIS F., YOURASSOWSKY C., MONNOM O., *et al.*, "Digital holographic microscopy for the three-dimensional dynamic analysis of in vitro cancer cell migration", *Journal of Biomedical Optics*, vol. 11, pp. 054032.1–054032.5, 2006.

[DUB 06c] DUBOIS F., CALLENS N., YOURASSOWSKY C., *et al.,* "Digital holographic microscopy with reduced spatial coherence for three-dimensional particle flow analysis", *Applied Optics*, vol. 45, pp. 864–871, 2006.

[DUB 12] DUBOIS F., YOURASSOWSKY C., "Full off-axis red-green-blue digital holographic microscope with LED illumination", *Optics Letters*, vol. 37, pp. 2190–2192, 2012.

[FER 04] FERRARO P., DE NICOLA S., COPPOLA G., *et al.*, "Controlling image size as a function of distance and wavelength in Fresnel-transform reconstruction of digital holograms", *Optics Letters*, vol. 29, pp. 854–856, 2004.

[FER 05] FERRARO P., GRILLI S., ALFIERI D., *et al.*, "Extended focused image in microscopy by digital holography", *Optics Express*, vol. 13, pp. 6738–6749, 2005.

[FER 06] FERRARO P., ALFERI D., DE NICOLA S., *et al.*, "Quantitative phase-contrast microscopy by a lateral shear approach to digital holographic image reconstruction", *Optics Letters*, vol. 31, pp. 1405–1407, 2006.

[GAB 48] GABOR D., "A new microscopic principle", *Nature*, vol. 161, pp. 777–778, 1948.

[GAB 49] GABOR D., "Microscopy by reconstructed wavefronts", *Proceedings of the Royal Society*, vol. A1947, p. 454, 1949.

[GAB 12] GABAI H., SHAKED N.T., "Dual-channel low-coherence interferometry and its application to quantitative phase imaging of fingerprints", *Optics Express*, vol. 20, pp. 26906–26912, 2012.

[GAR 06a] GARCIA-SUCERQUIA J., XU W., JERICHO M.H., *et al.*, "Immersion digital in-line holographic microscopy", *Optics Letters*, vol. 31, pp. 1211–1213, 2006.

[GAR 06b] GARCIA-SUCERQUIA J., XU W., JERICHO S.K., *et al.*, "Digital in-line holographic microscopy", *Applied Optics*, vol. 45, pp. 836–850, 2006.

[GHI 98] GHIGLIA D.C., PRITT M.D., *Two-dimensional Phase Unwrapping: Theory, Algorithms and Software*, Wiley, New York, 1998.

[GIR 13] GIRSHOVITZ P., SHAKED N.T., "Compact and portable low-coherence interferometer with off-axis geometry for quantitative phase microscopy and nanoscopy", *Optics Express*, vol. 21, pp. 5701–5714, 2013.

[GOO 67] GOODMAN J.W., LAWRENCE R.W., "Digital image formation from electronically detected holograms", *Applied Physics Letters*, vol. 11, pp. 77–79, 1967.

[GOO 85] GOODMAN J.W., *Statistical Optics*, Wiley, New York, 1985.

[GOO 05] GOODMAN J.W., *Introduction to Fourier Optics,* 3rd ed., Roberts & Company Publishers, Greenwood Village, 2005.

[GOO 07] GOODMAN J.W., *Speckle Phenomena in Optics*, Ben Roberts and Co, Swansea, 2007.

[GRE 84] GREIVENKAMP J.E., "Generalized data reduction for heterodyne interferometry", *Optical Engineering*, vol. 23, pp. 350–352, 1984.

[GRO 07] GROSS, M., ATLAN M., "Digital holography with ultimate sensitivity", *Optics Letters*, vol. 32, pp. 909–911, 2007.

[GRO 08] GROSS M., ATLAN M., ABSIL E., "Noise and aliases in off-axis and phase-shifting holography", *Applied Optics*, vol. 47, pp. 1757–1766, 2008.

[HAR 02] HARIHARAN P., *Basics of Holography*, Cambridge University Press, New York, 2002.

[HIN 02] HINSCH K.D., "Holographic particle image velocimetry", *Measurement Science and Technology*, vol. 13, pp. R61–R72, 2002.

[HUA 71] HUANG T.S., "Digital holography", *Proceedings of the IEEE*, vol. 159, pp. 1335–1346, 1971.

[KAR 12] KARRAY M., SLANGEN P., PICART P., "Comparison between digital Fresnel holography and digital image-plane holography: the role of the imaging aperture", *Experimental Mechanics*, vol. 52, pp. 1275–1286, 2012.

[KHM 08] KHMALADZE A., MARTÍNEZ A.R., KIM M., *et al.*, "Simultaneous dual wavelength reflection digital holography applied to the study of the porous coal samples", *Applied Optics*, vol. 47, pp. 3203–3210, 2008.

[KIM 99] KIM M.K., "Wavelength-scanning digital interference holography for optical section imaging", *Optics Letters*, vol. 24, pp. 1693–1695, 1999.

[KIM 11] KIM M., CHOI Y., FANG-YEN C., *et al.*, "High-speed synthetic aperture microscopy for live cell imaging", *Optics Letters*, vol. 36, pp. 148–150, 2011.

[KOU 07a] KOU S.S., SHEPPARD C.J., "Imaging in digital holographic microscopy", *Optics Express*, vol. 15, pp. 13640–13648, 2007.

[KOU 07b] KOU S.S., SHEPPARD C.J.R., "Comparison of three dimensional transfer function analysis of alternative phase imaging methods", *Biomedical Optics (BiOS)*, pp. 64430Q–64430Q-6, 2007.

[KRE 86] KREIS T., "Digital holographic interference-phase measurement using the Fourier-transform method", *Journal of the Optical Society of America A*, vol. 3, pp. 847–855, 1986.

[KRE 96] KREIS T., *Holographic Interferometry – Principles and Methods*, Akademie Verlag Gmbh, Berlin, 1996.

[KRE 97] KREIS T., ADAMS M., JÜPTNER W., "Methods of digital holography: a comparison", *Proceedings of SPIE*, vol. 3098, pp. 224–233, 1997.

[KRE 04] KREIS T., *Handbook of Holographic Interferometry Optical and Digital Methods*, Wiley-VCH, Weinheim, 2004.

[KRO 72] KRONROD M.A., MERZLYAKOV N.S., YAROSLAVSKII L.P., "Reconstruction of a hologram with a computer", *Soviet Physics Technical Physics*, vol. 17, pp. 333–334, 1972.

[KUH 07] KUHN J., COLOMB T., MONTFORT F., *et al.*, "Real-time dual-wavelength digital holographic microscopy with a single hologram acquisition", *Optics Express*, vol. 15, pp. 7231–7242, 2007.

[KUH 08] KUHN J., CHARRIERE F., COLOMB T., *et al.*, "Axial sub-nanometer accuracy in digital holographic microscopy", *Measurement Science and Technology*, vol. 19, p. 044007, 2008.

[KUH 09] KUHN J., MONTFORT F., COLOMB T., *et al.*, "Submicrometer tomography of cells by multiple-wavelength digital holographic microscopy in reflection", *Optics Letters*, vol. 34, pp. 653–655, 2009.

[KUM 09] KUMAR U.P., BHADURI B., KOTHIYAL M.P., *et al.*, "Two-wavelength microinterferometry for 3-D surface profiling", *Optics and Lasers in Engineering*, vol. 47, pp. 223–229, 2009.

[LAN 08] LANGEHANENBERG P., KEMPER B., DIRKSEN D., *et al.*, "Autofocusing in digital holographic phase contrast microscopy on pure phase objects for live cell imaging", *Applied Optics*, vol. 47, pp. D176–D182, 2008.

[LAU 02] LAUER V., "New approach to optical diffraction tomography yielding a vector equation of diffraction tomography and a novel tomographic microscope", *Journal of Microscopy*, vol. 205, pp. 165–176, 2002.

[LAU 10] LAUTERBORN W., KURZ T., *Coherent Optics: Fundamentals and Applications*, Springer-Verlag, Berlin, 2010.

[LE 00] LE CLERC F., COLLOT L., GROSS M., "Numerical heterodyne holography with two-dimensional photodetector arrays", *Optics Letters*, vol. 25, pp. 716–718, 2000.

[LE 01] LE CLERC F., GROSS M., COLLOT L., "Synthetic-aperture experiment in the visible with on-axis digital heterodyne holography", *Optics Letters*, vol. 26, pp. 1550–1552, 2001.

[LEC 13] LECLERCQ M., KARRAY M., ISNARD V., *et al.*, "Evaluation of surface acoustic waves on the human skin using quasi-time-averaged digital Fresnel holograms", *Applied Optics*, vol. 52, pp. A136–A146, 2013.

[LEE 13] LEE K., KIM K., JUNG J., *et al.*, "Quantitative phase imaging techniques for the study of cell pathophysiology: from principles to applications", *Sensors*, vol. 13, pp. 4170–4191, 2013.

[LI 07] LI J.C., PENG Z., FU Y., "Diffraction transfer function and its calculation of classic diffraction formula", *Optics Communications*, vol. 280, pp. 243–248, 2007.

[LI 09] LI J.C., TANKAM P., PENG Z., *et al.*, "Digital holographic reconstruction of large objects using a convolution approach and adjustable magnification", *Optics Letters*, vol. 34, pp. 572–574, 2009.

[LIE 03] LIEBLING M., BLU T., UNSER M., "Fresnelets: new multiresolution wavelet bases for digital holography", *IEEE Transaction on Image Processing*, vol. 12, pp. 29–43, 2003.

[LIE 04a] LIEBLING M., On Fresnelets, interferences fringes, and digital holography, PhD Thesis, no. 2977, Ecole Polytechnique Fédérale de Lausanne, Switzerland, 2004.

[LIE 04b] LIEBLING M., BLU T., UNSER M., "Complex-wave retrieval from a single off-axis hologram", *Journal of the Optical Society of America A*, vol. 21, pp. 367–377, 2004.

[LIE 04c] LIEBLING M., UNSER M., "Autofocus for digital Fresnel holograms by use of a Fresnelet-sparsity criterion", *Journal of the Optical Society of America A*, vol. 21, pp. 2424–2430, 2004.

[MAL 04] MALEK M., ALLANO D., COËTMELLEC S., *et al.*, "Digital in-line holography: influence of the shadow density on particle field extraction", *Optics Express*, vol. 12, pp. 2270–2279, 2004.

[MAN 05] MANN C., YU L., CHUN-MIN L., *et al.*, "High-resolution quantitative phase-contrast microscopy by digital holography", *Optics Express,* vol. 13, pp. 8693–8698, 2005.

[MAN 08] MANN C.J., BINGHAM P.R., PAQUIT V.C., *et al.*, "Quantitative phase imaging by three wavelength digital holography", *Optics Express*, vol. 16, pp. 9753–9764, 2008.

[MAR 93] MARRON J.C., SCHROEDER K.S., "Holographic laser-radar", *Optics Letters*, vol. 18, pp. 385–387, 1993.

[MAR 05] MARQUET P., RAPPAZ B., MAGISTRETTI P., *et al.*, "Digital holographic microscopy: a non-invasive contrast imaging technique allowing quantitative visualization of living cells with sub-wavelength axial accuracy", *Optics Letters*, vol. 30, pp. 468–470, 2005.

[MAR 13] MARQUET P., DEPEURSINGE C., MAGISTRETTI P.J., "Exploring neural cell dynamics with digital holographic microscopy", *Annual Review of Biomedical Engineering*, vol. 15, pp. 407–431, 2013.

[MAS 99] MAS D., GARCIA J., FERREIRA C., *et al.*, "Fast algorithms for free-space diffraction patterns calculation", *Optics Communications*, vol. 164, pp. 233–245, 1999.

[MAS 03] MAS D., PEREZ J., HERNANDEZ C., *et al.*, "Fast numerical calculation of Fresnel patterns in convergent systems", *Optics Communications,* vol. 227, pp. 245–258, 2003.

[MAS 05] MASSATSCH P., CHARRIERE F., CUCHE E., *et al.*, "Time-domain optical coherence tomography with digital holographic microscopy", *Applied Optics*, vol. 44, pp. 1806–1812, 2005.

[MON 06] MONTFORT F., COLOMB T., CHARRIERE F., *et al.*, "Submicrometer optical tomography by multiple-wavelength digital holographic microscopy", *Applied Optics*, vol. 5, pp. 8209–8217, 2006.

[MUN 10] MUNDT J., KREIS T.M., "Digital holographic recording and reconstruction of large scale objects for metrology and display", *Optical Engineering*, vol. 49, pp. 125801-1–125801-6, 2010.

[ONU 92] ONURAL L., OZGEN M.T., "Extraction of three-dimensional object-location information directly from in-line holograms using Wigner analysis", *Journal of the Optical Society of America A*, vol. 9, pp. 252–260, 1992.

[ONU 93] ONURAL L., "Diffraction from a wavelet point of view", *Optics Letters*, vol. 18, pp. 846–848, 1993.

[PAR 12] PARTHASARATHY A.B., CHU K.K, FORD T.N., *et al.*, "Quantitative phase imaging using a partitioned detection aperture", *Optics Letters*, vol. 37, pp. 4062–4064, 2012.

[PED 95] PEDRINI G., TIZIANI H.J., "Digital double pulse holographic interferometry using Fresnel and image plane holograms", *Measurement*, vol. 18, pp. 251–260, 1995.

[PED 02] PEDRINI G., TIZIANI H.J., "Short-coherence digital microscopy by use of a lens less holographic imaging system", *Applied Optics*, vol. 41, pp. 4489–4496, 2002.

[PIC 03] PICART P., LEVAL J., MOUNIER D., *et al.*, "Time-averaged digital holography", *Optics Letters*, vol. 28, pp. 1900–1902, 2003.

[PIC 05] PICART P., LEVAL J., MOUNIER D., *et al.*, "Some opportunities for vibration analysis with time averaging in digital Fresnel holography", *Applied Optics*, vol. 44, pp. 337–343, 2005.

[PIC 08] PICART P., LEVAL J., "General theoretical formulation of image formation in digital Fresnel holography", *Journal of the Optical Society of America A*, vol. 25, pp. 1744–1761, 2008.

[PIC 09] PICART P., TANKAM P., MOUNIER D., *et al.*, "Spatial bandwidth extended reconstruction for digital color Fresnel holograms", *Optics Express*, vol. 17, pp. 9145–9156, 2009.

[PIC 12] PICART P., LI J.C., *Digital Holography*, ISTE, London and John Wiley & Sons, New York, 2012.

[PIC 13a] PICART P., TANKAM P., "Analysis and adaptation of convolution algorithms to reconstruct extended objects in digital holography", *Applied Optics*, vol. 52, pp. A240–A253, 2013.

[PIC 13b] PICART P., MALEK M., "Complex field recovering from in-line digital holography", *Optics Letters*, vol. 38, pp. 3230–3232, 2013.

[RAJ 14] RAJSHEKHAR G., BHADURI B., EDWARDS C., *et al.*, "Nanoscale topography and spatial light modulator characterization using wide-field quantitative phase imaging", *Optics Express*, vol. 22, pp. 3432–3438, 2014.

[RES 10] RESTREPO J.F., GARCIA-SUCERQUIA J., "Magnified reconstruction of digitally recorded holograms by Fresnel-Bluestein transform", *Applied Optics*, vol. 49, pp. 6430–6435, 2010.

[SAM 11] SAMSON B., VERPILLAT F., GROSS M., *et al.*, "Video-rate laser Doppler vibrometry by heterodyne holography", *Optics Letters*, vol. 36, pp. 1449–1451, 2011.

[SCH 94] SCHNARS U., JÜPTNER W., "Direct recording of holograms by a CCD target and numerical reconstruction", *Applied Optics*, vol. 33, pp. 179–181, 1994.

[SCH 96] SCHNARS U., KREIS T.M., JÜPTNER W., "Digital recording and numerical reconstruction of holograms: reduction of the spatial frequency spectrum", *Optical Engineering*, vol. 35, pp. 977–982, 1996.

[SCH 99] SCHEDIN S., PEDRINI G., TIZIANI H.J., *et al.*, "Simultaneous three-dimensional dynamic deformation measurements with pulsed digital holography", *Applied Optics*, vol. 38, pp. 7056–7062, 1999.

[SEE 01] SEEBACHER S., OSTEN W., BAUMBACH T., *et al.*, "The determination of material parameters of microcomponents using digital holography", *Optics and Lasers in Engineering*, vol. 36, pp. 103–126, 2001.

[SHA 10] SHAFFER E., MORATAL C., MAGISTRETTI P., *et al.*, "Label-free second-harmonic phase imaging of biological specimen by digital holographic microscopy", *Optics Letters*, vol. 35, pp. 4102–4104, 2010.

[SHE 10] SHEPPARD C.J.R., KOU S.S., "3D imaging with holographic tomography", *AIP Conference Proceedings*, vol. 1236, p. 65, 2010.

[SIE 86] SIEGMAN A.E., *Laser*, University Science Books, Sausalito Cal., 1986.

[SIN 10] SINGH D.K., PANIGRAHI P.K., "Improved digital holographic reconstruction algorithm for depth error reduction and elimination of out-of-focus particles", *Optics Express*, vol. 18, pp. 2426–2448, 2010.

[SLA 84] SLANEY M., KAK A.C., LARSEN L.E., "Limitations of imaging with first-order diffraction tomography", *IEEE Transactions on Microwave Theory and Techniques*, vol. 32, p. 860, 1984.

[SUN 09] SUNG Y.J., CHOI W., FANG-YEN C., *et al.*, "Optical diffraction tomography for high resolution live cell imaging", *Optics Express*, vol. 17, pp. 266–277, 2009.

[TAK 82] TAKEDA M., INA H., KOBAYASHI S., "Fourier-transform method of fringe-pattern analysis for computed-based topography and interferometry", *Journal of the Optical Society of America*, vol. 72, pp. 156–160, 1982.

[TAN 10a] TANKAM P., SONG Q., KARRAY M., *et al.*, "Real-time three-sensitivity measurements based on three-color digital Fresnel holographic interferometry", *Optics Letters*, vol. 35, pp. 2055–2057, 2010.

[TAN 10b] TANKAM P., PICART P., MOUNIER D., *et al.*, "Method of digital holographic recording and reconstruction using a stacked color image sensor", *Applied Optics*, vol. 49, pp. 320–328, 2010.

[TAN 11] TANKAM P., PICART P., "Use of digital color holography for crack investigation in electronic components", *Optics and Lasers in Engineering*, vol. 49, pp. 1335–1342, 2011.

[VER 10] VERRIER N., REMACHA C., BRUNEL M., *et al.*, "Micropipe flow visualization using digital in-line holographic microscopy", *Optics Express*, vol. 18, pp. 7807–7819, 2010.

[WOL 69] WOLF E, "Three-dimensional structure determination of semi-transparent objects from holographic data", *Optics Communications*, vol. 1, pp. 153–156, 1969.

[WYA 75] WYANT J.C., "Use of an ac heterodyne lateral shear interferometer with real-time wavefront correction systems", *Applied Optics*, vol. 14, pp. 2622–2626, 1975.

[YAM 97] YAMAGUCHI I., ZHANG T., "Phase-shifting digital holography", *Optics Letters*, vol. 22, pp. 1268–1270, 1997.

[YAM 01a] YAMAGUCHI I., KATO J., OHTA S., *et al.*, "Image formation in phase shifting digital holography and application to microscopy", *Applied Optics*, vol. 40, pp. 6177–6186, 2001.

[YAM 01b] YAMAGUCHI I., KATO J., OHTA S., "Surface shape measurement by phase shifting digital holography", *Optical Review*, vol. 8, pp. 85–89, 2001.

[YAM 02] YAMAGUCHI I., MATSUMURA T., KATO J., "Phase shifting color digital holography", *Optics Letters*, vol. 27, pp. 1108–1110, 2002.

[YAR 85] YARIV A., *Optical Electronics*, Holt, Rinehart and Winston, New York, 1985.

[YOU 14] YOURASSOWSKY C., DUBOIS F., "High throughput holographic imaging-in-flow for the analysis of a wide plankton size range", *Optics Express*, vol. 22, pp. 6661–6673, 2014.

[YU 05] YU L., KIM M.K., "Wavelength-scanning digital interference holography for tomographic three-dimensional imaging by use of the angular spectrum method", *Optics Letters*, vol. 30, pp. 2092–2094, 2005.

[ZHA 98] ZHANG T., YAMAGUCHI I., "Three-dimensional microscopy with phase shifting digital holography", *Optics Letters*, vol. 23, pp. 1221–1223, 1998.

[ZHA 04] ZHANG F., YAMAGUCHI I., "Algorithm for reconstruction of digital holograms with adjustable magnification", *Optics Letters*, vol. 29, pp. 1668–1670, 2004.

[ZHA 08] ZHAO J., JIANG H., DI J., "Recording and reconstruction of a color holographic image by using digital lensless Fourier transform holography", *Optics Express*, vol. 16, pp. 2514–2519, 2008.